

<b>REPORT DOCUMENTATION PAGE</b>				Form Approved OMB NO. 0704-0188	
<p>The public reporting burden for this collection of information is estimated to average 1 hour per response, including the time for reviewing instructions, searching existing data sources, gathering and maintaining the data needed, and completing and reviewing the collection of information. Send comments regarding this burden estimate or any other aspect of this collection of information, including suggestions for reducing this burden, to Washington Headquarters Services, Directorate for Information Operations and Reports, 1215 Jefferson Davis Highway, Suite 1204, Arlington VA, 22202-4302. Respondents should be aware that notwithstanding any other provision of law, no person shall be subject to any penalty for failing to comply with a collection of information if it does not display a currently valid OMB control number.</p> <p>PLEASE DO NOT RETURN YOUR FORM TO THE ABOVE ADDRESS.</p>					
1. REPORT DATE (DD-MM-YYYY)		2. REPORT TYPE Technical Report		3. DATES COVERED (From - To) -	
4. TITLE AND SUBTITLE MEASUREMENT OF AEROSOL OPTICAL PROPERTIES BY INTEGRATING CAVITY RING-DOWN SPECTROSCOPY AND NEPHELOMETERY				5a. CONTRACT NUMBER W911NF-11-1-0188	
				5b. GRANT NUMBER	
				5c. PROGRAM ELEMENT NUMBER 206022	
6. AUTHORS Getachew Tedela				5d. PROJECT NUMBER	
				5e. TASK NUMBER	
				5f. WORK UNIT NUMBER	
7. PERFORMING ORGANIZATION NAMES AND ADDRESSES North Carolina A&T State University 1601 East Market Street  Greensboro, NC 27411 -3209				8. PERFORMING ORGANIZATION REPORT NUMBER	
9. SPONSORING/MONITORING AGENCY NAME(S) AND ADDRESS(ES) U.S. Army Research Office P.O. Box 12211 Research Triangle Park, NC 27709-2211				10. SPONSOR/MONITOR'S ACRONYM(S) ARO	
				11. SPONSOR/MONITOR'S REPORT NUMBER(S) 58934-PH-REP.6	
12. DISTRIBUTION AVAILABILITY STATEMENT Approved for public release; distribution is unlimited.					
13. SUPPLEMENTARY NOTES The views, opinions and/or findings contained in this report are those of the author(s) and should not be construed as an official Department of the Army position, policy or decision, unless so designated by other documentation.					
14. ABSTRACT We measure scattering coefficient, extinction coefficient, scattering cross-section and single scattering albedo of 102, 203 and 296 polystyrene spheres by integrating cavity ring-down spectroscopy and nephelometry in order to calibrate the system for further studies of biomass aerosols. We compared experimental optical property measurements with Mie theory predicted values. The scattering coefficient and scattering cross-section measurements of the 203 and 296 nm polystyrene spheres agree with Mie theory predictions with uncertainty of <					
15. SUBJECT TERMS CRD, Nephelometry					
16. SECURITY CLASSIFICATION OF:			17. LIMITATION OF ABSTRACT UU	15. NUMBER OF PAGES	19a. NAME OF RESPONSIBLE PERSON Solomon Bililign
a. REPORT UU	b. ABSTRACT UU	c. THIS PAGE UU			19b. TELEPHONE NUMBER 336-285-2328

## **Report Title**

# **MEASUREMENT OF AEROSOL OPTICAL PROPERTIES BY INTEGRATING CAVITY RING-DOWN SPECTROSCOPY AND NEPHELOMETERY**

## **ABSTRACT**

We measure scattering coefficient, extinction coefficient, scattering cross-section and single scattering albedo of 102, 203 and 296 polystyrene spheres by integrating cavity ring-down spectroscopy and nephelometry in order to calibrate the system for further studies of biomass aerosols. We compared experimental optical property measurements with Mie theory predicted values. The scattering coefficient and scattering cross-section measurements of the 203 and 296 nm polystyrene spheres agree with Mie theory predictions with uncertainty of < 1% and <3% respectively. The optical property measurement for 102 nm polystyrene spheres however disagrees from 9-30%. Single scattering albedo values for the 203 and 296 nm polystyrene spheres are > 0.8. The Single scattering albedo for the 102 nm polystyrene spheres ranges from 0.6 to 1. As the scattering measurements are done with less uncertainty for the 203 and 296 nm polystyrene spheres, possible cause for underestimation of the single scattering albedo could be the higher extinction coefficient measured by the CRD. The major sources of errors are discussed and recommendations made to improve accuracy for future measurements.

MEASUREMENT OF AEROSOL OPTICAL PROPERTIES BY  
INTEGRATING CAVITY RING-DOWN SPECTROSCOPY AND  
NEPHELOMETER

by

Getachew Tedla

A project submitted to the graduate faculty  
in partial fulfillment of the requirements for the degree of  
MASTER OF SCIENCE

Department: Physics  
Major: Physics  
Major Professor: Dr. Solomon Bililign

North Carolina A&T State University  
Greensboro, North Carolina  
2013

## Table of contents

### Contents

Table of contents.....	2
ABSTRACT.....	3
ACKNOWLEDGMENT.....	4
Chapter 1- Introductions and Background.....	8
1.1 Aerosol formation mechanisms .....	9
1.2 Atmospheric effect of Aerosols .....	11
Chapter 2- Scattering and extinction measurement .....	20
2.1 Mie theory .....	21
2.2 Integrating nephelometer .....	23
2.3 Extinction measurement.....	27
<b>CHAPTER 3- EXPERIMENT</b> .....	29
<b>CHAPTER-4- RESULTS</b> .....	35
4.1 Scattering measurement before calibration.....	35
4.2 Particle loss measurement.....	41
4.3 Scattering measurement using a recalibrated system.....	42
4.4 Extinction measurement.....	49
<b>CHAPTER 5- DISCUSSION</b> .....	65
5.1. Comparison with Mie theory calculations .....	65
5.2. Calibration gas uncertainty .....	67
5.3. Effects of water vapor.....	67
5.4. Photon counting uncertainty .....	68
5.5. Nephelometer angular non-ideality.....	68
5.6 Uncertainty in extinction measurements.....	69
5.7 Uncertainty in single scattering albedo.....	73
Chapter 6 –Conclusion and recommendations .....	74
<b>BIBLIOGRAPHY</b> .....	76

## **ABSTRACT**

We measure scattering coefficient, extinction coefficient, scattering cross-section and single scattering albedo of 102, 203 and 296 polystyrene spheres by integrating cavity ring-down spectroscopy and nephelometry in order to calibrate the system for further studies of biomass aerosols. We compared experimental optical property measurements with Mie theory predicted values. The scattering coefficient and scattering cross-section measurements of the 203 and 296 nm polystyrene spheres agree with Mie theory predictions with uncertainty of  $< 1\%$  and  $< 3\%$  respectively. The optical property measurement for 102 nm polystyrene spheres however disagrees from 9-30%. The optical property measurement for 102 nm polystyrene spheres however disagrees from 9-30%. Single scattering albedo values for the 203 and 296 nm polystyrene spheres are  $> 0.8$ . The Single scattering albedo for the 102 nm polystyrene spheres ranges from 0.6 to 1. As the scattering measurements are done with less uncertainty for the 203 and 296 nm polystyrene spheres, possible cause for underestimation of the single scattering albedo could be the higher extinction coefficient measured by the CRD. The major sources of errors are discussed and recommendations made to improve accuracy in future measurements.

## **ACKNOWLEDGMENT**

The author gratefully acknowledges the financial support from the Department of Defense, Grant #W911NF-11-1-0188, Dr. Solomon Bililign for his valuable comments on the manuscript for giving the author an opportunity to work as a research assistant in his group. The author also gratefully acknowledges extreme willingness of Dr. Marc Fiddler to share his immense experiment skills and his availability for discussion and guidance. It is a pleasant experience to work with Sujeeta Singh in the lab and thanks for valuable discussion.

## List of Tables

Table 1 Testing the nephelometer sensitivity for room Aerosols and for blank cavity (by covering its inlet using the HEPA filter).....	37
Table 2 Experimental and theoretical comparisons of total scattering and scattering cross-sections of 103 nm particles at 589 nm, for different concentrations with a blower fitted to the nephelometer.....	37
Table 3 Experimental and theoretical comparisons of total scattering and scattering cross-sections of 296 nm particles at 589 nm for different concentrations with a blower fitted to the nephelometer.....	37
Table 4 Particle loss measurement within the nephelometer with and without external Blower for 102 and 296 nm polystyrene spheres. ....	42
Table 5 Particles loss measurement, for 102 and 296 nm polystyrene spheres, across the Cavity .....	42
Table 6 Theoretical and experimental total scattering and scattering cross-section of 102 nm polystyrene spheres at 589 nm without the blower .....	44
Table 7 Theoretical and experimental total scattering and scattering cross-section for 203 nm Polystyrene spheres at 589 nm without the blower .....	44
Table 8 Theoretical and experimental total scattering and scattering cross-section for 296 nm polystyrene spheres at 589 nm without the blower .....	45
Table 9 extinction coefficient, single scattering albedo and extinction cross-section of 296, 102 and 203 nm particles.....	64

## List of Figures

Figure 1 Global particle emission for the year 2000 in (Tg/Year). <a href="http://www.geo.tu-darmstadt.de/fg/umweltmin/umwelt_forschung/forschungsseiten/atmospheric_aerosolparticles.de.jsp">http://www.geo.tu-darmstadt.de/fg/umweltmin/umwelt_forschung/forschungsseiten/atmospheric_aerosolparticles.de.jsp</a> .....	9
Figure 2 Experimental set up extinction and scattering coefficient measurements using CRD and nephelometer .....	34
Figure 3 Averaging time and blank time estimation to calibrate the nephelometer (Horizontal axis-time change in seconds, vertical axis- total scattering (in $\text{m}^{-1}$ ) (Green-450 nm, Blue-550, red 700 nm wavelength). ....	38
Figure 4. Scatter plots to estimate the scattering coefficient at 589 nm wavelength, using the scattering coefficient measured at 450, 550 and 700 nm wavelengths for 102 nm size particles when an external blower is fitted to the nephelometer. ....	39
Figure 5. Scatter plots to estimate the scattering coefficient at 589 nm wavelength, using the scattering coefficient measured at 450, 550 and 700 nm wavelengths for 296 nm size particles when an external blower is fitted to the nephelometer. ....	40
Figure 6. Scatter plots to estimate the scattering coefficient at 589 nm wavelength, using the scattering coefficient measured at 450, 550 and 700 nm wavelengths for 102 nm size particles without external blower.....	46
Figure 7. Scatter plots to estimate the scattering coefficient at 589 nm wavelength, using the scattering coefficient measured at 450, 550 and 700 nm wavelengths for 203 nm size particles without external blower.....	47

Figure 8. Scatter plots to estimate the scattering coefficient at 589 nm wavelength, using the scattering coefficient measured at 450, 550 and 700 nm wavelengths for 296 nm size particles without external blower.....	48
Figure 9 Ring down time of water vapor and 102 nm Polystyrene latex spheres as a function of wavelength.....	50
Figure 10 Ring down time of water vapor and 203 nm Polystyrene latex spheres as a function of wavelength.....	51
Figure 11 Ring down time of water vapor and 296 nm Polystyrene latex spheres as a function of wavelength.....	51
Figure 12. Extinction coefficient of 103 nm Polystyrene latex spheres using CRD as a function of wavelength in nm .....	52
Figure 13 Extinction coefficient of 203 nm Polystyrene latex spheres using CRD as a function of wavelength in nm .....	52
Figure 14 Extinction coefficient of 296 nm Polystyrene latex spheres using CRD as a function of wavelength in nm .....	53
Figure 15. Spectra of 102 nm polystyrene latex spheres with fitted trend regression line to estimate the extinction coefficient (1st measurement) . X axis is logarithm of the wave length and the y axis is logarithm of extinction coefficient. ....	54
Figure 16. Spectra of 102 nm polystyrene latex spheres with fitted trend regression line to estimate the extinction coefficient (2nd measurement) . X axis is logarithm of the wave length and the y axis is logarithm of extinction coefficient. ....	54
Figure 17. Spectra of 102 nm polystyrene latex spheres with fitted trend regression line to estimate the extinction coefficient (3rd measurement) . X axis is logarithm of the wave length and the y axis is logarithm of extinction coefficient. ....	55
Figure 18. Spectra of 102 nm polystyrene latex spheres with fitted trend regression line to estimate the extinction coefficient (4th measurement) . X axis is logarithm of the wave length and the y axis is logarithm of extinction coefficient. ....	55
Figure 19. Spectra of 102 nm polystyrene latex spheres with fitted trend regression line to estimate the extinction coefficient (5th measurement) . X axis is logarithm of the wave length and the y axis is logarithm of extinction coefficient. ....	56
Figure 20. Spectra of 203 nm polystyrene latex spheres with fitted trend regression line to estimate the extinction coefficient (1st measurement) . X axis is logarithm of the wave length and the y axis is logarithm of extinction coefficient. ....	57
Figure 21. Spectra of 203 nm polystyrene latex spheres with fitted trend regression line to estimate the extinction coefficient (2nd measurement) . X axis is logarithm of the wave length and the y axis is logarithm of extinction coefficient. ....	57
Figure 22. Spectra of 203 nm polystyrene latex spheres with fitted trend regression line to estimate the extinction coefficient (3rd measurement) . X axis is logarithm of the wave length and the y axis is logarithm of extinction coefficient. ....	58
Figure 23. Spectra of 203 nm polystyrene latex spheres with fitted trend regression line to estimate the extinction coefficient (4th measurement) . X axis is logarithm of the wave length and the y axis is logarithm of extinction coefficient. ....	58
Figure 24. Spectra of 203 nm polystyrene latex spheres with fitted trend regression line to estimate the extinction coefficient (5th measurement) . X axis is logarithm of the wave length and the y axis is logarithm of extinction coefficient. ....	59



Figure 25. Spectra of 203 nm polystyrene latex spheres with fitted trend regression line to estimate the extinction coefficient (6th measurement) . X axis is logarithm of the wave length and the y axis is logarithm of extinction coefficient. ....	59
Figure 26. Spectra of 296 nm polystyrene latex spheres with fitted trend regression line to estimate the extinction coefficient (First measurement) . X axis is logarithm of the wave length and the y axis is logarithm of extinction coefficient. ....	60
Figure 27. Spectra of 296 nm polystyrene latex spheres with fitted trend regression line to estimate the extinction coefficient (second measurement) . X axis is logarithm of the wave length and the y axis is logarithm of extinction coefficient. ....	60
Figure 28. Spectra of 296 nm polystyrene latex spheres with fitted trend regression line to estimate the extinction coefficient (5th measurement) . X axis is logarithm of the wave length and the y axis is logarithm of extinction coefficient. ....	62
Figure 29. Spectra of 296 nm polystyrene latex spheres with fitted trend regression line to estimate the extinction coefficient (6th measurement) . X axis is logarithm of the wave length and the y axis is logarithm of extinction coefficient. ....	62

## **CHAPTER 1- INTRODUCTIONS AND BACKGROUND**

Atmospheric aerosols are suspensions of solid and/or liquid particles in air. They are ubiquitous in air and are often observable as dust, smoke, and haze [1]. Both natural and human processes contribute to aerosol concentrations that differ considerably in their size ranges and chemical composition.

Aerosols from natural sources include; sea-salt aerosols, aerosols formed in atmosphere from a gaseous phase, dust aerosols, biological aerosol, aerosols from forest fires and volcanic aerosol. Anthropogenic aerosols mainly result from biomass burning and from a variety of combustion sources due to industrialization (Figure 1). Aerosols can be emitted directly (primary aerosols) or formed from gaseous species in the atmosphere (secondary aerosol). They can be organic, inorganic, biological, or a mixture thereof.

Aerosols may affect human health, visibility, weather and climate. The acute health responses that have been associated with air pollution due to aerosols include respiratory and lung disease including coughing or asthma attacks, cardiac symptoms such as angina attacks, disabilities, and absences from work or school, due to hospitalization, and ultimately premature mortality [2]. For instance, the 1955 “killer Fog” that enveloped over London, England resulted in 1000 deaths, and a different London smog incident killed 750 people in 1962. Similarly, in Donora, Pennsylvania, the 1948 air pollution episode killed 20 people and numerous animals, and half of the town's 12,000 residents become ill due to uncontrolled emissions from industrial facilities [3]. Aerosols can also

affect the visibility in the atmosphere depending on their concentration and nature. Poor visibility could have adverse effect on transportation and communication in general.

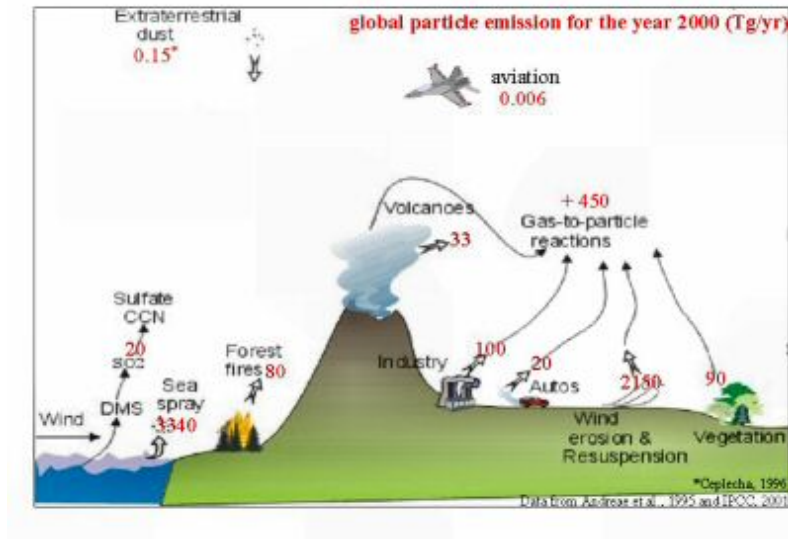


**Figure 1 Global particle emission for the year 2000 in (Tg/Year).** [http://www.geo.tu-darmstadt.de/fg/umweltmin/umwelt\\_forschung/forschungsseiten/atmosphericaerosolparticles.de.jsp](http://www.geo.tu-darmstadt.de/fg/umweltmin/umwelt_forschung/forschungsseiten/atmosphericaerosolparticles.de.jsp)

## 1.1 Aerosol formation mechanisms

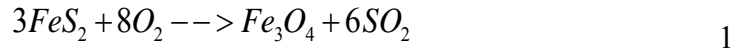
There are different mechanisms that lead to aerosol formation in the atmosphere. For instance trace gases can be converted in to less volatile products or condense on existing particles to cause particle growth, or they can condense spontaneously to form new particles. This process is called nucleation. For example sulfuric acid vapor and highly oxidized organic gases may lead to new particle formation through nucleation. The other process is the formation of particles from coagulation of smaller particles. This mode of formation is called accumulation. Mechanical forces can also give rise to the formation of large and smaller particles. For instance, dust formation by wind action can result in

small and larger particles. Such a process of formation is referred to as coarse mode aerosol formation.

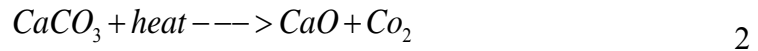
Aerosols are broadly classified by their chemical compositions as: soot particles, mineral dust, sulfate particles, organic particles, and sea salt particles.

Soot particles contain elemental carbon in the form of very small particles, aggregated together, and formed by combustion of fossil fuels and biomass burning such as forest fires and agricultural burning. Mineral dust is formed from storms over arid areas such as the Sahara desert. Dust particles can be transported several thousand kilometers such as from Asia to North America. Iron oxide, silica and carbonates are some examples of dust minerals that can easily be coated with sulfates and organic compounds. Sulfate aerosols contain sulfate ion formed from the oxidation of sulfur compounds. Over continents,  $\text{SO}_2$  formed from the combustion of fossil fuels is the major source for sulfate aerosols.  $\text{SO}_2$  can be changed to sulfuric acid in the presence of OH to form sulfuric acid that condenses by gas-particle conversion process. In the presence of ammonia, sulfuric acid can be converted to ammonium sulfate aerosols. Sea salt aerosols are formed when bubble braking occurs at the surface of ocean. Organic aerosols are emitted both by pollution and biogenic sources. isoprenes and terpenes are examples of organic compounds emitted to the atmosphere by plants. Although initially volatile these molecules can be transformed in to soluble species and further they can be converted through the gas-particle conversion processes.

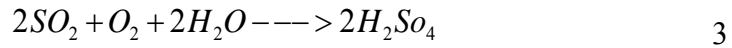
A detailed chemical reactions on aerosol formation processes and on heterogeneous chemistry can be found in [4] [5]. Below we provide some examples of aerosol formation mechanisms from coal. For instance a mineral dust such as iron oxide aerosol particles can be formed during the combustion of pyrite-containing coal.



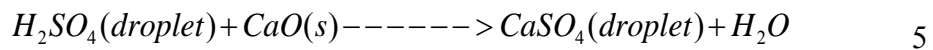
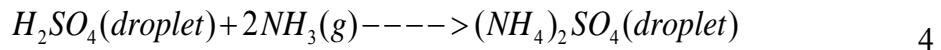
similarly calcium carbonate in the ash fraction of coal can be converted to calcium oxide and could be emitted to the atmosphere:



Another common process for the formation of aerosols involves the oxidation of atmospheric sulfur dioxide to sulfuric acid, a hygroscopic substance that accumulates atmospheric water vapor to form small liquid droplets:



In the presence of ammonia or calcium oxide the sulfuric acid reacts to form salts



Under low-humidity conditions water exhausts from these droplets and a solid aerosol forms.

## 1.2 Atmospheric effect of Aerosols

It is known that atmospheric aerosol particles play, a direct or indirect, role in regulation of Earth's radiation balance. The direct effect of aerosols is typically characterized by the absorption and scattering of incoming shortwave and outgoing long wave radiation.

Aerosol can have a cooling and warming effect in the atmosphere depending on their tendency to absorb and make the atmosphere warmer or scatter the energy back to space and eventually cool the planet. While the warming effect complements the effect of greenhouse gases, the cooling effect of aerosols tends to offset the warming associated with greenhouse gases.

Depending on their nature, the atmospheric aerosols could also alter cloud cover and cloud properties [6] which is considered as an indirect effect, that changes the microphysical properties of clouds, by serving as cloud condensation nuclei.

Accurate measurement of optical properties of aerosols is crucial for quantifying the influence of aerosols on climate. The ability of aerosols to interact with radiation is dictated by their optical properties, which depend on their physical and chemical characteristics, and on the wavelength of the incident light [7]. The optical properties relevant for estimating the direct effects of aerosols are; scattering and absorption coefficients ( $\alpha_{sc}$ ,  $\alpha_{ab}$ ); extinction cross-sections  $\sigma_{ext}$  [8]; aerosol optical thickness (loading); phase function (angular dependence of light scattering), absorption efficiency  $Q_{abs}$  and single-scattering albedo ( $\omega$ ) [9]. The single-scattering albedo determines the sign (depending whether it does have a cooling or heating effect) of the aerosol radiative forcing, while the asymmetry of the phase function together with optical thickness of the atmospheric aerosol help to drive the magnitude of forcing [9].

Absorption and scattering efficiencies are the ratio of absorption and scattering cross-section to geometric cross-section:

$$Q_{abs/sc} = \frac{\sigma_{abs/sc}}{\sigma_{geom}} \quad (6)$$

For spherical particles, the geometric cross-section is given by  $\sigma_{geom} = \pi r^2$ . For an ensemble of  $N$  suspended particles, the absorption coefficient is the sum of the individual absorption cross-sections divided by the volume  $V$  occupied by the ensemble. For identical particles, this simplifies to the product of particle number density  $N$  and the particle absorption cross-section [10].

$$\alpha_{abs/sc} = \frac{\sum_{i=1}^n \sigma_{abs/sc\_i}}{V} = N \sigma_{abs/sc}; N = \frac{n}{V} \quad (7)$$

The single scattering albedo is the ratio of scattering cross-section to the extinction cross-section, which is the sum of the scattering and absorption cross-sections.

$$\omega = \frac{\sigma_{sca}}{\sigma_{ext}} = \frac{\sigma_{sca}}{\sigma_{sca} + \sigma_{abs}} \quad (8)$$

The wavelength dependence of aerosol scattering/absorption properties can also be expressed using the scattering/absorption coefficients  $\alpha_{s/a}$  and the Angstrom scattering/absorption coefficient  $\Delta$  as:

$$A_{s/a}^o = - \frac{\log\left(\frac{\alpha_{s/a}(\lambda_1)}{\alpha_{s/a}(\lambda_2)}\right)}{\log\left(\frac{\lambda_1}{\lambda_2}\right)} \quad (9)$$

The magnitude of particle scattering or absorption of electromagnetic waves is dependent on the wavelength of the incident light  $\lambda$ , the size of the particle  $D_p$ , and the index of refraction of the material  $m$ , where

$$m = n + ik \quad (10)$$

and  $n$  is the real part and  $k$  is the imaginary part of the index of refraction. The size parameter  $x$

$$x = \frac{\pi D_p}{\lambda} \quad (11)$$

is a dimensionless parameter which is often used to describe the relationship between the particle size and the wavelength of the incident light.

Absorbing aerosol types include urban pollution, biomass burning, desert dust and mixtures [11]. Some of these atmospheric aerosols absorb more solar radiation than the others; specifically carbonaceous particles and mineral dust are typically characterized by a strong absorption. For instance, black carbon with a deep black appearance, which is caused by a significant, non-zero imaginary part  $k$  (i.e 0.79) of the refractive index shows wavelength independent absorption over the visible and near-visible spectral regions (i.e Absorption Angstrom Coefficient, AAC=1) [10]. Brown carbon, another absorbing aerosol type, is a class of light-absorbing carbonaceous material, which unlike black carbon has an imaginary part  $k$  of its refractive index  $m$  that increases towards shorter visible and ultraviolet (UV) wavelengths (much higher than 1 AAC) has brownish or yellowish visual appearance [10]. On the other hand, light scattering particles have high reflectivity; nearly zero or extremely low absorption of incoming atmospheric radiation. Highly reflective aerosol particles have a nearly zero imaginary part of the complex



refractive index. These particles generally have a cooling effect on the atmosphere. Examples are sea salt particles, white polystyrene latex spheres,  $\text{CuCl}_2 \cdot 2\text{H}_2\text{O}$ , pure nitrate and ammonium sulphate  $(\text{NH}_4)_2\text{SO}_4$  compounds.

The complexity of quantifying the effect that aerosols have on local and regional climate increases substantially when one considers how optical properties change as aerosols mix and when the atmosphere changes. According to the IPCC's Fourth Assessment Report, the ability to quantify the direct effect of aerosols on the global climate is hindered by uncertainties in the measurements of aerosol extinction.

Therefore, characterizing aerosol climate forcing is a complex problem. Moreover, modeling and understanding the effect of aerosol in the climate forcing becomes more difficult as the aerosol have immense diversity, not only in spatial and temporal distribution but also in particle size, composition, and origin. Aerosol composition can be highly variable, with different species present within the same particle, due to different sources, production mechanisms, and chemical transformations.[12].

Aerosol optical properties can be measured from space using satellites and aircrafts, ambient measurement by installing equipment outdoor or using indoor laboratory installations. In most measurement schemes, careful calibration of measuring equipment is a crucial step in the process.

Laboratory calibrations can provide a misleading perception of accuracies that can be achieved when an instrument is used to measure optical properties of atmospheric aerosols. Similar instruments that have been carefully calibrated in the laboratory may disagree when used for ambient aerosol measurements due to subtle difference in size cuts, or different sensitivities to aerosol hygroscopic properties, particle density or hygroscopicity [13]. While such calibration tools permit precise assessments of instrument responses to known laboratory-generated aerosols, unquantifiable uncertainties remain even when carefully calibrated instruments are used for atmospheric measurements [13]. This is because instrument responses typically depend on aerosol properties including composition, shape, density, etc., which, for atmospheric aerosols, may vary from particle-to-particle and are often unknown. Therefore more effort needs to be made to quantify measurement accuracies that can be achieved for realistic atmospheric sampling scenarios [13]

Well-calibrated system enables to achieve a reliable and reproducible result. On the other hand, if equipments are not correctly calibrated, uncertainties in measured optical properties or number density may lead to an over estimation, underestimation of final radiative, or climate related models.

For instance, as reported on [9], single scattering albedo of desert dust simulated, according to a number of models, ranges from 0.63 to 0.87 at  $0.5 \mu\text{m}$ , such uncertainty is big, since even smaller changes of the scattering albedo (from 0.95 to 0.85) would change the radiative forcing of desert dust from significant cooling to significant warming [9].

Several instruments are available for aerosol optical property measurement. Scattering component of light extinction by aerosols is often characterized using different types of integrating nephelometers. For instance, TSI Inc. Model 3561 performs scattering measurement at 550 nm wavelength, and Model 3563 functions at three (450, 550, and 700 nm) wavelengths. Other types of integrating nephelometers are also discussed in [14].

Other aerosol optical property measuring devices include cavity ring-down spectrometer (CRD) to measure light extinction and photo-acoustic absorption spectrometer (PAS) for light absorption. Cavity ring-down (CRD) spectroscopy is a direct absorption technique, which can be performed with pulsed or continuous light sources and has a significantly higher sensitivity than obtainable in conventional absorption spectroscopy [15]. The CRD technique is based upon the measurement of the rate of absorption rather than the magnitude of absorption of a light pulse confined in a closed optical cavity with a high Q factor [15]. The advantage over normal absorption spectroscopy results from, the intrinsic insensitivity to light source intensity fluctuations and, secondly, the extremely long effective path lengths (many kilometers) that can be realized in stable optical cavities [15].

An integrated measurement of scattering and absorption coefficients using nephelometer, CRD and theoretical simulation using Mie theory (see section 2) has been a tool to estimate aerosol optical properties. Such integrated system has been tested to measure

extinction with well-characterized laboratory generated aerosols, and measured extinctions agree within 5% of predictions by Mie theory [16]. Single scattering albedo measurement for different dry smokes have been conducted also by [17]. They measured the absorption coefficient, using a photoacoustic spectrometer and scattering coefficient measurements using a TSI 3563 nephelometer. Their results indicated that the single scattering albedo varied from 0.43–0.99, indicative of the wide variations in smoke aerosol chemical composition.

The type and sources of errors for an integrated system may differ depending on the equipment design and the working principles of the instruments. The focus of this project is, therefore, to calibrate aerosol optical property measuring devices; integrating nephelometer, cavity ring-down spectroscopy, particle density and size measuring instruments implemented to study optical properties of biomass burning aerosols. Calibrating instruments is a very crucial step in experimental studies, which enables correction of uncertainties of measurement by comparing experimental result with theoretical simulations.

The project focuses on calibrating cavity ring-down spectroscopy and nephelometer using different size polystyrene spheres that includes the following results:

1. Comparison of nephelometer measurement with Mie theory calculations

2. Calculated single scattering albedo of polystyrene spheres from scattering coefficient obtained using nephelometer and the extinction coefficient measured using a cavity ring-down spectroscopy
3. Comparing experimental results with literature values
4. Identify sources of errors and introduces correction factors to nephelometer, CRD, particle size and number density measurements.

## CHAPTER 2- SCATTERING AND EXTINCTION MEASUREMENT

Scattering is the redirection of solar radiation out of its original direction of propagation due to interactions with particles. The scattering could take place in the form of reflection, refraction, diffraction etc.

Parameters that govern the scattering behavior are wavelength of the incident radiation  $\lambda$ , the particle optical properties relative to the surrounding medium (the complex refractive index) and the size of the scattering particle, which is expressed as the non-dimensional size parameter  $x$ .

Depending on the size parameter, there are three scattering regions:

1.  $x \ll 1$  rayleigh scattering
2.  $x \sim$  Mie scattering
3.  $x \gg 1$  geometric scattering

As the scattering and extinction measurements done in this project are mainly with in the Mie region, below a brief description of the Mie theory is discussed and the Rayleigh scattering is included in the theory of the integrating nephelometer as part of the scattering due to the calibrating span gases.

## 2.1 Mie theory

Mie scattering is a theoretical simulation method to characterize light scattering behavior for homogenous spherical particles. The scattering calculations are done using Maxwell's equations to derive the wave equation for electromagnetic radiation in space expressed in spherical coordinates with appropriate boundary conditions at the surface of the sphere. The solutions are expressed as infinite series of products of cosines and sines for the dependence on  $\Phi$ , spherical Bessel functions for the dependence on  $r$  and associated Legendre polynomials for dependence on cosine  $\theta$ . Detail derivation routines can be found on [18].

Extinction and scattering efficiencies are expressed in terms of the scattering coefficients  $a_n$  and  $b_n$  which are functions of  $x$  and  $m$  as:

$$\begin{aligned} Q_e &= \frac{2}{x^2} \sum_{n=1}^{\infty} (2n+1) \text{Re}(a_n + b_n) \\ Q_s &= \frac{2}{x^2} \sum_{n=1}^{\infty} (2n+1) (|a_n|^2 + |b_n|^2) \end{aligned} \quad (12)$$

Theoretical Mie scattering results indicate that the extinction efficiency is generally small in Rayleigh limit and largest when the scattering particles and wavelengths have similar size. The Mie scattering theory is applicable for size parameter that ranges from  $0.1 < x < 100$ .

Besides the extinction efficiencies, Mie theory is a powerful tool to describe the change in scattering coefficient of aerosol with respect to water content [19], to calculate the effective refractive indices of aerosols [20], the extinction coefficients, cross sections of aerosols [16] and the phase function (the angular distribution of light intensity scattered by a particle at a given wavelength). A number of Mie algorithms code compiled in different computer languages can be found on [21]. Most Algorithms work by computing the scattering coefficients,  $a_n$  and  $b_n$ , from the size parameter and the index of refraction  $m$  using the recursion relations for spherical Bessel functions. Then from the Mie scattering coefficients the algorithms compute  $Q_e$  and  $Q_s$  using the above equations.

Closure between measured optical signals and those Mie calculated from concurrent measurements of size distributions is the basis of well-conducted aerosol–optical inter comparisons [22]. For that purpose the uncertainties of measured and calculated properties must be evaluated. Several studies have estimated the total uncertainty in the scattering measurements of the TSI instruments at somewhere around 10% [23, 24] [25].

Mie calculations have shown that truncation errors resulting from sub- $\mu\text{m}$  particles are small and well correlated with the wavelength dependence of their scattering, while truncation errors for super- $\mu\text{m}$  particles are large and poorly correlated with the wavelength dependence of their scattering [26] [27].

For non-spherical particles more complex scattering codes are needed to calculate truncation errors as a function of particle shape and size. Examples of such codes are the



discrete-dipole approximation for the calculation of scattering from particles of arbitrary shape [28] and codes based on rigorous solutions extended from Mie theory for agglomerate particles [20, 21][27].

## **2.2 Integrating nephelometer**

Integrating nephelometer is one of the most sensitive equipment that enables to measure scattering coefficient in the order of  $10^{-7} \text{ m}^{-1}$ . The integrating nephelometer performs a geometrical integration of the angular distribution of scattered light intensity such that the scattering coefficient of a gaseous or aerosol medium can be measured with the combination of a Lambertian light source and an orthogonal light detector [29]. It was first devised by [30] and improved further by different developers (example [29]).

Major assumptions inherent in integrating nephelometer designs are: (a) that the illumination is Lambertian (isotropic) over all angles, (b) that the light source dimension is small compared to length of the sensing volume, and (c) that the forward and backward (near 0 and 180 degree) truncation limits of the angular integration are small. To the degree that these assumptions are not met the measured scattering coefficient may be in error and needs to be corrected [31].

The effect of the non-idealities was that the measured scattering coefficient could generally be less than the true value and that this systematic error is strongly dependent on particle size and more significant for particles larger than 1 micrometer in diameter [31].

The total scattering  $S_{ts}$  and backscattering signal  $S_{bs}$  measured by integrating nephelometer at wavelength  $\lambda$  can be written as:

$$\begin{aligned}
 S_{ts,\lambda} &= \int_0^{180} F_{\lambda}(\theta) Z_{ts}(\theta) d\theta \\
 S_{bs,\lambda} &= \int_0^{180} F_{\lambda}(\theta) Z_{bs}(\theta) d\theta
 \end{aligned} \tag{13}$$

Where  $\theta$  is the scattering angle,  $F_{\lambda}(\theta)$  is the scattering function,  $Z_{ts}(\theta)$  and  $Z_{bs}(\theta)$  are the angular sensitivity functions of the nephelometer for total scattering and back scattering respectively and expressed in terms of  $\theta$  as.

$$\begin{aligned}
 Z_{ts} &= \sin(\theta) \\
 Z_{bs} &= \begin{cases} \sin(\theta) & 90 < \theta < 180 \\ 0 & otherwise \end{cases}
 \end{aligned} \tag{14}$$

The angular scattering function of particle population and the carrier gas  $F_{\lambda}(\theta)$  is expressed in terms of the particle number size distribution  $dn(d_p)/d\log d_p$ , and the angular scattering function of individual particles  $F_{\lambda}(\theta, m_{\lambda}, d_p)$  which is a function of complex refractive index  $m_{\lambda}$  and diameter  $d_p$ .  $F_{\lambda}$  is usually calculated from scattering codes and used as an integrand in the expression for  $F_{\lambda}(\theta)$  which is expressed as:

$$F_{\lambda}(\theta) = \int_{-\infty}^{\infty} f_{\lambda}(\theta, m_{\lambda}, d_p) \frac{dn(d_p)}{d \log d_p} \pi \left( \frac{d_p}{2} \right)^2 d \log d_p + F_R(\theta) \quad (16)$$

$F_R(\theta)$  is the contribution of the Rayleigh scattering of the carrier gas to the scattering function. Calibration of integrating nephelometer with two particle free gases of known Rayleigh total and back scattering coefficients ( $\sigma_{tsR}$ ,  $\sigma_{bsR}$ ) yields calibration constants  $K$ , which relate scattering signals  $S$  to total scattering and back scattering coefficients  $\sigma_{ts}$  and  $\sigma_{bs}$

$$\begin{aligned} \sigma_{ts,\lambda} &= K_{ts,\lambda} S_{ts,\lambda} - \sigma_{tsR,\lambda} \\ \sigma_{bs,\lambda} &= K_{bs,\lambda} S_{bs,\lambda} - \sigma_{bsR,\lambda} \end{aligned} \quad (17)$$

The contribution for Rayleigh scattering are calculated analytically for a given temperature and pressure and subtracted from the scattering signals [32]. Detailed derivation routine on the physics of integrating nephelometer can be found on [32, 33].

Therefore, besides to the uncertainty sources due to the basic assumptions in integrating nephelometer, measurement error could be introduced due to high relative humidity, temperature and pressure changes as described below.

### 1. Calibration gas uncertainty:

The scattering coefficient of a gas varies with temperature T and Pressure P according to the ideal gas law

$$\sigma_{K-gas} = \sigma_{K-gas(STP)} \left( \frac{273.3}{T} \right) \left( \frac{P}{1013.2} \right) \quad (18)$$

Where, the standard temperature and pressure (STP) are 273.2 k and 1013.2 mb respectively. The above expression indicates that at constant temperature the scattering coefficient of a gas increases with pressure. The scattering coefficient also decreases when the temperature increases keeping the pressure constant.

### 2. Effects of water vapor

The effect of water vapor on scattering coefficient is proportional to the fraction of water molecules in the gas. The ratio of the scattering coefficient for a wet particle to the scattering coefficient when it is dry is expressed by:

$$\frac{\sigma_{K-wet}}{\sigma_{K-dry}} = 1 - \eta \frac{e}{P} = 1 - \eta \frac{e_{s(T)}}{P} \frac{RH}{100} \quad (19)$$

Where  $e_{s(T)}$  is the saturation water pressure at temperature T and RH is the relative humidity. The water vapor correction factor  $\eta$ , accounts for the refractive index and depolarization effects. Assuming water vapor and standard dry air to have same depolarization factor of 1.05, the correction factor is  $\eta = 0.31$ .

### 3. Photon counting uncertainty

Photon-counting uncertainties affect both measurement noise and accuracy. The conversion from raw count ( $C_{\text{raw}}$ ) to scaled count ( $C_s$ ) in terms of averaging time ( $\tau$ ) and gate width  $G$  (see TSI reference manual) is given by

$$C_s = \frac{C_{\text{raw}}}{\tau} \frac{360^0}{G} \quad (20)$$

The uncertainty in photon count ( $\delta C$ ) for each of the three types of scaled counts is given by

$$\delta C^2 = \frac{2 \times 360 \times C_s}{\tau G} \quad (21)$$

## 2.3 Extinction measurement

One of the most important advantages of cavity ring-down spectroscopy measurements in analytical measurements is its high sensitivity. Recent advances allow for detection of absorbance as low as  $10^{-9}$  [26]. In a pulsed cavity ring-down experiment a laser pulse is introduced in to an optical cavity containing a pair of high reflectivity mirrors. The light intensity decays exponentially in time, with a time constant  $\tau$ , due to losses within the cavity because of absorption, scattering, and both mechanisms or due to loss at the mirrors. The decay time is called the ring-down time. Extinction is then determined from the temporal decay of the light intensity measured at one end of the cavity. The light intensity transmitted through the mirrors as a function of time is described by:

$$I = I_o \text{Exp}\left(\frac{t}{\tau}\right) \quad (18)$$

Extinction due to scattering and absorption by gases and particles reduces the lifetime of light within the cavity. The extinction coefficient,  $\sigma_e$ , is expressed in terms of the ratio of optical cavity length to the length of cavity filled with a sample ( $RL$ ), the speed of light ( $c$ ), the ring-down time constant for a sample filled cavity ( $\tau$ ), and the ring-down time constant of a blank cavity ( $\tau_0$ ):

$$\sigma_e = \frac{RL}{c} \left( \frac{1}{\tau} - \frac{1}{\tau_o} \right) \quad (19)$$

Sources of error and uncertainty in measuring aerosol optical properties using CRD has been discussed in detail in [34]. For instance measurement uncertainty of the length of cavity occupied by aerosol may result about 2.5% error of retrieved refractive index (for  $RL = 1.14$ ). Condensation particle counting efficiency of  $\pm 10\%$  leads to 2.5% error, on the other hand  $\pm 6\text{nm}$  errors in diameter can result refractive index uncertainty up to 2.9%. Presence of nanometer-thick absorbed layers on particle surface can lead between 0.3-4% size dependent errors in retrieved refractive index. Doubly and triply charged particles passing through the DMA can also cause measurement uncertainty when particles are selected from polydispersed aerosol distribution.

The ability to measure precisely minimal differences in ring down times between an empty cavity  $\tau_o$  and a cavity filled with aerosols  $\tau$  provides a good estimate of the maximum sensitivity. The minimum detectable extinction coefficient is expressed in

terms of length of the cavity  $L$ , the actual distance in the cavity filled with a sample  $D$  and the standard deviation of the decay time  $\Delta\tau_{\min}$  [16]:

$$\alpha_{\min} = \frac{L}{c \times D} \frac{\Delta\tau_{\min}}{\tau_o} \quad (20)$$

## CHAPTER 3- EXPERIMENT

The main purpose of this work is to calibrate the integrating nephelometer and the cavity ring-down spectroscope, it is therefore imperative to choose aerosol particles having a perfect scattering property and representative in size to the atmospheric aerosols. For that purpose, commercial polystyrene spheres having a mean diameter of 296, 203 and 102 nm and a microsphere density of  $1.05\text{gm/cm}^3$  with a similar refractive index of  $m=1.59+0i$  at 589 nm was obtained from Duke scientific corporation. To insure statistically consistent sampling, the solution was dispersed thoroughly by immersing in a lower ultrasonic bath for 10 seconds.

Aqueous solutions of the polystyrene latex spheres are nebulized using a TSI constant output atomizer (TSI-3076) in a recirculation mode, which is recommended for water-based solutions. As drying and neutralizing the aerosol is the most important factors for quality atomizing, dry particle-free pure nitrogen has been used at a pressure of less than 35 psi, with a flow rate of  $\sim 3.25$  standard liters per minute (SLM) to generate a mono disperse particle droplets. The aerosol then passed through silica gel diffusion dryer (TSI-3062) to remove bounded water.

The dried aerosols pass through a Scanning Mobility Particle Sizer (SMPS) that contains Model 3080 Electrostatic classifier with nano differential mobility analyzer and with an impactor inlet. The classifier has a wide range of scanning capability that ranges from 2 to 1000 nm particles. Since our aerosols samples are monodisperse particles with known size, we set diameter to 103, 206 and 296 nm. A powerful feature of the classifier is that one can directly enter a particle diameter and the nearest voltage setting will appear in the



voltage pane and the DMA voltage will be controlled to that setting. For particle density measurement we use TSI's N-WCPC Model 3788. This sophisticated particle counter utilizes state-of-the art water based condensation technology with lowest detectable particle size of the water based condensation particle counter (WCPC) family. The Model 3788 can measure up to  $4 \times 10^5$  particles/cm<sup>3</sup> single particle counting and has sheath flow with high aerosol flow rate.

The laser components of the system include, A Continuum surelite I-20, Nd:YAG laser with 4-6 ns pulse width and  $1 \text{ cm}^{-1}$  line width at 20 Hz frequency and an ND6000 dye laser with a grating line width of  $0.08 \text{ cm}^{-1}$  at 560 nm. We use Rhodamine 610 dye at 53.5 mg and 18.7 mg in 500 mL methanol solution for the amplifier and the oscillator respectively. A second harmonic of the Nd: YAG at 532 nm pumped the dye laser. The laser is tuned at 589 nm wavelength and calibrated using a wave meter. The laser was focused in to the cavity using an iris, polarizer wave-plate, a two lenses telescope, a pinhole and two turning mirrors as depicted in Figure 2. Helium Neon laser (HeNe) was used to align the cavity with the dye laser using the turning mirrors to assure the desired mode matching within the cavity. Finally a high reflecting mirror with a reflectivity of 99.995% at 620 nm wavelength mounted at the two ends of the cavity and aligned to optimize the ring-down time. A small purge flow of dry particle free nitrogen is introduced in front of each mirror to prevent the mirrors from contamination by deposition of aerosols and moisture.

To measure the ratio of the cavity length to the distance occupied by the sample, first we estimated  $\tau_o$  for a blank cavity, and then we measure the ring down time for ozone filled cavity with nitrogen purge flow  $\tau_N$  and without purge flow  $\tau_F$ . Then we calculated  $R_L$  using the equation:

$$R_L = \frac{\left( \frac{1}{\tau_F} - \frac{1}{\tau_o} \right)}{\left( \frac{1}{\tau_N} - \frac{1}{\tau_o} \right)} \quad (21)$$

Sensitivity of the nephelometer increases by the square root of the averaging time. For instance, to double the sensitivity, the sampling time should be quadrupled. When testing for a blank nephelometer, averaging time can be set to a lower value to decrease the response time, but in the presence of aerosols a longer averaging time is necessary to increase the nephelometer's sensitivity.

In order to quantify the nephelometer uncertainty, first we conducted total and back scattering measurement as calibration done by the manufacturer, for room aerosols and for blank cavity by covering the nephelometer inlet with a high-efficiency particulate air (HEPA). For this test we set an averaging time of 5 seconds, blanking time of 30 seconds and an auto zero period of 3600 seconds. During the room aerosol measurement we used an external blower to draw sample in to the measurement volume.

Then we connected the nephelometer to the cavity ring-down setup and the condensation particle counter as shown in Figure 2. In the presence of polystyrene aerosol samples, we set averaging time to 120 seconds, the auto zero measurement time to 240 seconds and

the blank value to 700 seconds. As the nephelometer switches between clean and sample air during blanking time, the data in this transition period has not been used. During the auto zero period the nephelometer checks changes in instrument background due to contaminants and we set it to 3600 seconds. When the nephelometer was connected to the CPC, the blower was off and the particles have been drawn to the measurement volume by the CPC.

With the calibration done by the manufacturer we measured the total scattering coefficient for the three different size polystyrene spheres at 450, 550 and 700 nm wavelengths using the nephelometer, the extinction coefficient using the CRD and corresponding number density using the CPC.

As particle number density is a crucial parameter in estimating the scattering coefficient, we measured particle concentrations at different positions of the system to identify the amount of potential losses. To keep the stability of particle flow, we started measuring from the outlet of the nephelometer, then the cavity outlet and finally the DMA outlet. The difference between nephelometer outlet and the cavity outlet reading will indicate the amount of particle loss within the nephelometer. The DMA outlet reading and that of the cavity outlet will indicate the particle loss within the cavity.

After measuring the scattering coefficient as well as the extinction coefficient for 103 and 296 nm polystyrene latex spheres as calibrated by the manufacturer, we made a new calibration using two span gases; air (low span gas) and CO<sub>2</sub> for the high span gas. To do

so, we follow the 15 step procedures indicated in the reference manual [35]. After the total scatter calibration constant of the reference chopper reads in the order of  $10^{-3}$  and the backscatter calibration constant of the reference chopper reads in the order of  $10^{-1}$  in  $\text{m}^{-1}$ , desired values as indicated on the TSI reference manual, we write the new values to the nephelometer.

After calibrating the nephelometer with air and high span gas ( $\text{CO}_2$ ) we made a clean air test by changing the valve position parameter to zero and the measured scattering coefficient values were in the order of  $10^{-7}$  and  $10^{-8}$  indicating a good calibration of the nephelometer.

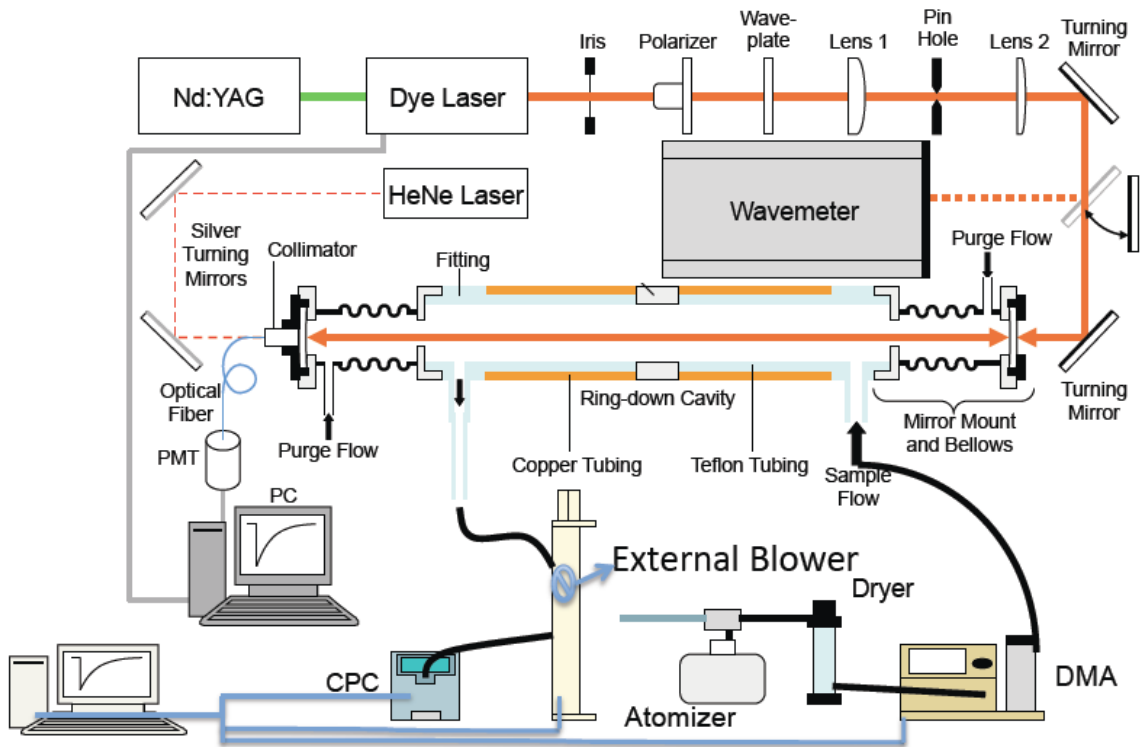


**Figure 2** Experimental set up extinction and scattering coefficient measurements using CRD and nephelometer

## CHAPTER-4- RESULTS

### 4.1 Scattering measurement before calibration

As indicated in (Table 1), the scattering coefficient measurement for room aerosols and when the inlet of the nephelometer was covered by the HEPA filter indicate differences in the order of  $10^{-2}$ . These measurements were done as the calibration performed by the manufacturer. Although the measurement with fitted HEPA filter seems reasonable, i.e. nearly zero readings, the measurements for room aerosols are not certain since seeing room aerosols having scattering coefficient in the order of  $10^{-5}$  was not expected. Therefore, we decided to measure scattering coefficient of 102 and 296 nm size polystyrene latex spheres using the same calibration procedures done by the manufacturer and see how those values compare to theoretical predictions.

Since the ultimate objective is to calibrate the CRD and nephelometer for integrated aerosol optical property measurements, estimation and predictions of the two systems has to be synchronized for the same wavelength.

The nephelometer reading is strictly limited to 450, 550 and 700 nm wavelengths; we used scatter plots of the logarithm of wavelengths versus the logarithm of total scattering, to predict the scattering coefficient at 589 nm wavelength. This scatter plot approach is similar to calculating the Angstrom coefficient at two different wavelengths except in the scatter approach instead of considering two wavelengths; we consider all the three wavelengths.

As indicated in Figure 3, we estimated the total scattering coefficient for the 102 nm particles by conducting five consecutive experiments. This increases statistically the accuracy of scattering coefficient and scattering cross-section measurements. Although all are fitted to a linear regression line, they have different slopes and intercepts. As the slopes are related to angstrom coefficient, the estimated scattering coefficients will vary accordingly.

The predicted scattering coefficient of 103 nm Polystyrene particles varies from  $2.72836 \times 10^{-07}$  to  $6.07723 \times 10^{-07} \text{ m}^{-1}$  (Table 2). The scattering cross-section also varies from  $1.21325 \times 10^{-16}$  to  $2.67723 \times 10^{-16}$ . Comparisons with Mie predicted scattering coefficient and scattering cross-section indicated percentage errors that range from 19.5 to 45.8 % (Table 2).

For 296 nm particles, the estimated scattering coefficients and scattering cross-sections is somehow closer to theoretical predictions. As indicated in Figure 5, the deviation between the slopes of the five different measurements is lower than those indicated on Figure 4. The percent errors of scattering coefficient and scattering cross-section from Mie theory predictions range from 16.56 - 18.15% (Table 3). These values are much lower and narrower in range than what is observed for the 102 nm particles. Even though the theoretical and experimental comparisons are better for the 296 nm particles, percentage error of 16-18% is quite big, as the particles are perfectly spherical and perfectly scattering particles. In order to see the development of those uncertainties in cross-sections, first we investigated the amount of particle loss across the nephelometer.

	Room Aerosol		HEPA Filter	
	Total Scatter	Backscatter	Total Scatter	Backscatter
Blue	1.36E-5 to 9.66E-6	3.01E-6 to 2.00E-6	5.75E-7 to 5.85E-7	1.16E-6 to 3.59E-7
Green	8.42E-6 to 5.96E-6	1.55E-6 to 8.26E-7	-5.78E-8 to -7.72E-7	-3.94E-8 to -4.36E-7
Red	5.03E-6 to 3.66E-6	1.65E-6 to 9.61E-7	-7.49E-8 to -7.27E-7	3.67E-7 to -3.48E-8

**Table 1 Testing the nephelometer sensitivity for room Aerosols and for blank cavity (by covering its inlet using the HEPA filter).**

Experi #	$\lambda$ in nm	Experi.		Experi.	Mie-X- section	Mie Total scatter	%Err-X-sec	%Err-Total scatter
		Total-Scatter	Particles/cc	X-sec				
1	589	3.23443E-07	2292	1.41132E-16	2.24E-16	5.13E-07	3.70E+01	37.0
2	589	6.07723E-07	2270	2.67723E-16	2.24E-16	5.08E-07	1.95E+01	19.6
3	589	2.72836E-07	2249	1.21325E-16	2.24E-16	5.04E-07	4.58E+01	45.8
4	589	3.43338E-07	2225	1.54338E-16	2.24E-16	4.98E-07	3.11E+01	31.1
5	589	3.40942E-07	2221	1.53501E-16	2.24E-16	4.98E-07	3.15E+01	31.5

**Table 2 Experimental and theoretical comparisons of total scattering and scattering cross-sections of 103 nm particles at 589 nm, for different concentrations with a blower fitted to the nephelometer**

Experi #	$\lambda$ in nm	Experi.		Experi.		Mie-Total scatter	%Err-X-sec	%Err-Total scatter
		Total-Scat	Particles/cc	X-sec	Mie-Xsec			
1	589	2.05783E-05	264	7.79E-14	9.523E-14	0.00002514	18.1	18.1
2	589	2.07584E-05	261	7.94E-14	9.523E-14	0.0000249	16.6	16.6
3	589	2.07756E-05	260	7.98E-14	9.523E-14	0.00002478	16.2	16.1
4	589	2.03785E-05	261	7.84E-14	9.523E-14	0.0000247	17.6	17.5
5	589	2.06633E-05	260	7.95E-14	9.523E-14	0.00002476	16.7	16.6

**Table 3 Experimental and theoretical comparisons of total scattering and scattering cross-sections of 296 nm particles at 589 nm for different concentrations with a blower fitted to the nephelometer**

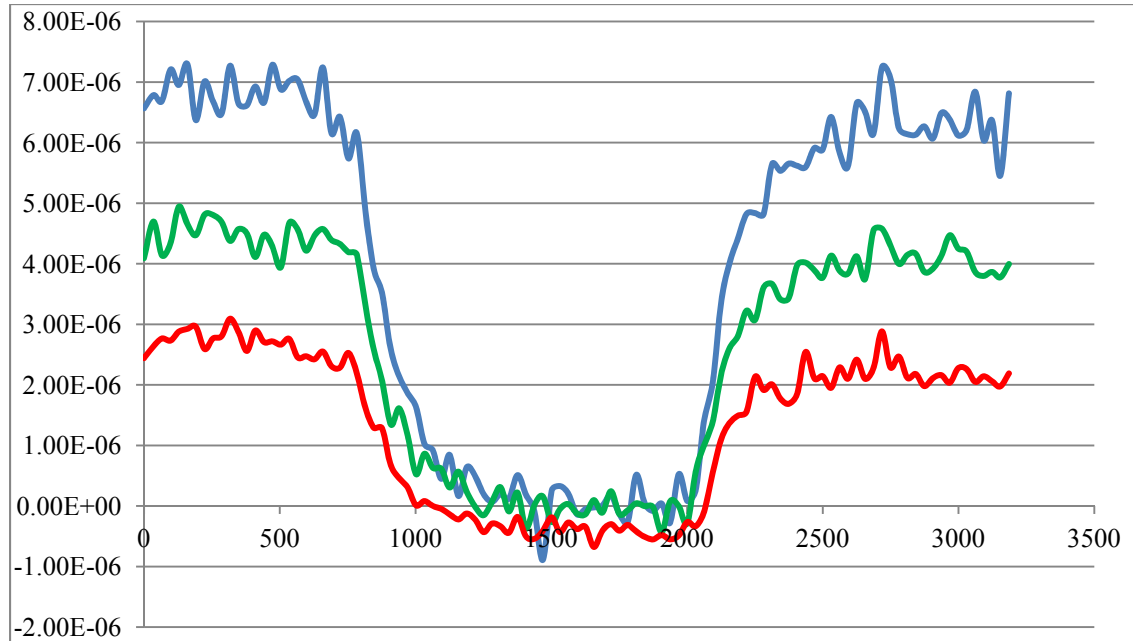
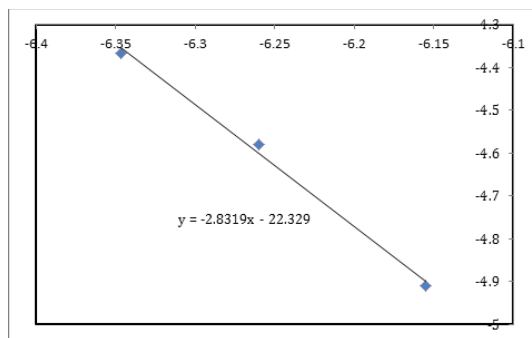
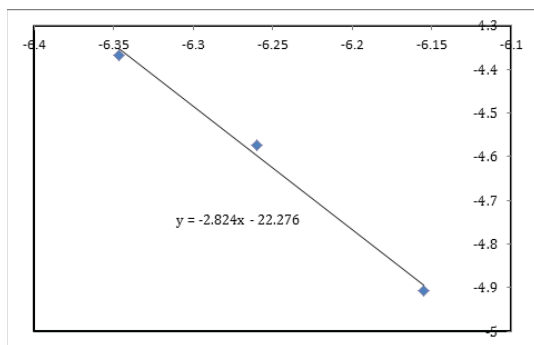


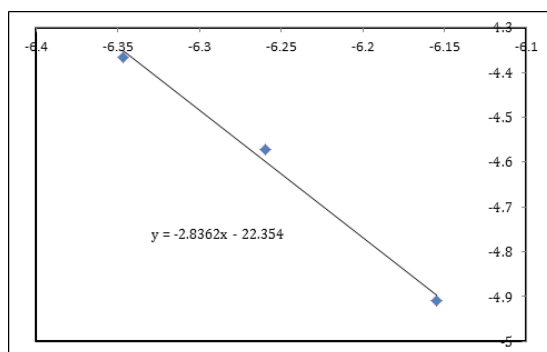
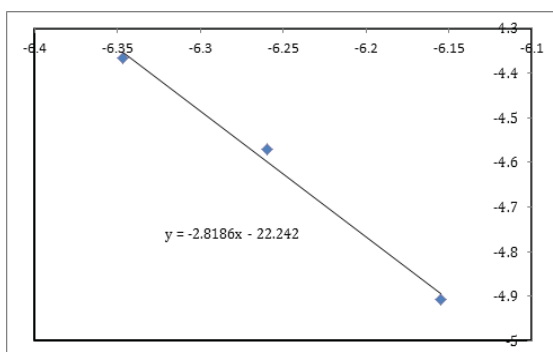
**Figure 3 Averaging time and blank time estimation to calibrate the nephelometer** (Horizontal axis-time change in seconds, vertical axis- total scattering (in  $\text{m}^{-1}$ ) ( Green-450 nm, Blue-550, red 700 nm wavelength).





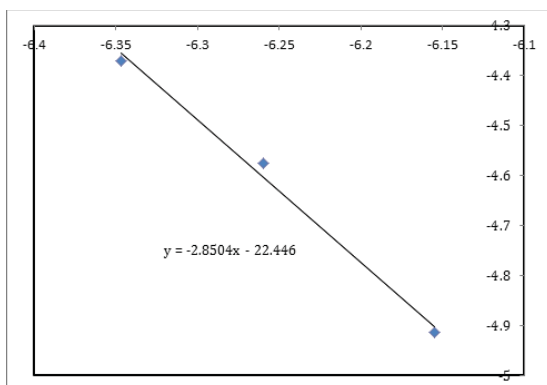
A

B



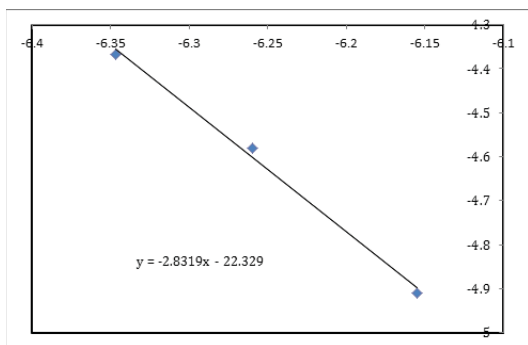
C

D

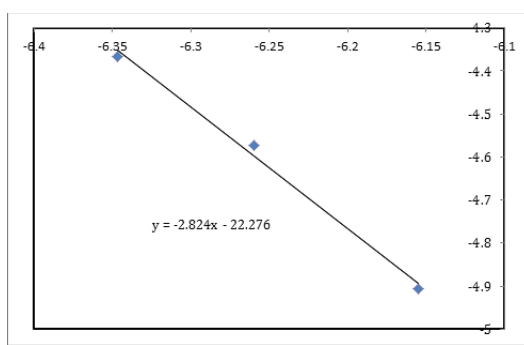


E

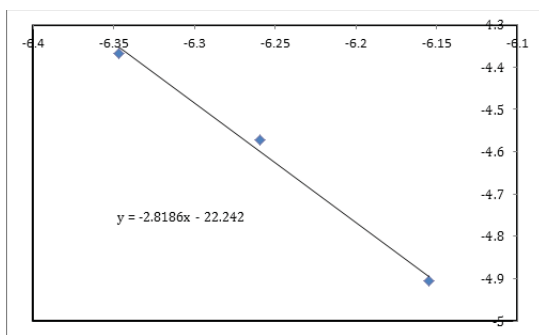
**Figure 4. Scatter plots to estimate the scattering coefficient at 589 nm wavelength, using the scattering coefficient measured at 450, 550 and 700 nm wavelengths for 102 nm size particles when an external blower is fitted to the nephelometer.**



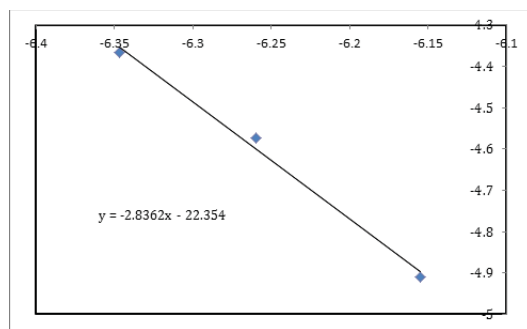
A



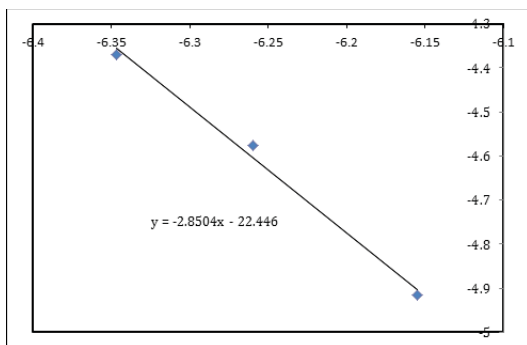
B



C



D



E

**Figure 5. Scatter plots to estimate the scattering coefficient at 589 nm wavelength, using the scattering coefficient measured at 450, 550 and 700 nm wavelengths for 296 nm size particles when an external blower is fitted to the nephelometer.**

## 4.2 Particle loss measurement

The previous measurement was done with an external blower fitted to the nephelometer. In the next approach we had to check the effect of an external blower on the particle concentrations within the nephelometer when measurement is taking place. The particle loss in the nephelometer when the external blower was fitted was 36% for the 102 nm polystyrene spheres and 16% for the 296 nm spheres. When the blower was removed and using the CPC to draw the aerosol particles into the measurement volume, the percent loss across the nephelometer decreased to 16.5 and 9.7 % for the 102 and 296 nm polystyrene particles respectively (Table 4). Our observation is that, the external blower affects the particle concentration within the nephelometer. Another point noticed is, that particle loss is more pronounced for the 102nm particles than for the 296 nm particles.

Similarly we conducted particle concentration measurement within the cavity, and indeed particle loss across the cavity also depends on aerosol size. As indicated in Table 5, the loss for 102 nm particles was 10% and for the 296 nm polystyrene spheres it was 0.5 %. Nevertheless, particle loss within the cavity is lower than loss observed within the nephelometer (Table 4; Table 5).

As all the observed percent error might not be accounted for the particle loss alone, we decided to recalibrate the nephelometer using span gases and by extracting the blank and averaging time parameters from a scattering coefficient versus time change graph

(Figure 3).

Size PLS	Neph. Outlet	Neph. Inlet	Loss %
102 nm	2080	3262	36
296 nm	176	208	16
Without Blower			
Size PLS	Neph. Outlet	Neph. inlet	
102 nm	2413	2890	17
296 nm	222	246	10

**Table 4 Particle loss measurement within the nephelometer with and without external Blower for 102 and 296 nm polystyrene spheres.**

Size PLS	Cavity outlet	Cavity inlet	Loss in %
102 nm	3262	3641	10
296 nm	208	209	0.6

**Table 5 Particles loss measurement, for 102 and 296 nm polystyrene spheres, across the Cavity**

### 4.3 Scattering measurement using a recalibrated system

When we remove the external blower and recalibrate the nephelometer using the span gases (gases used to calibrate our system), we found quite different results in measurement. As indicated in Figure 6, Figure 7 and Figure 8, the deviations among slopes of the different measurements are lower than what is indicated in Figure 4 and Figure 5.

Furthermore the percentage error between measured and Mie theory based predictions of the 102 nm particles range from 9.38 to 32.2% for scattering cross-sections and from 9.49 to 32.25 for scattering coefficient (Table 6). This range is narrower than before and the values are much lower.

For the 203 nm polystyrene particles, the percentage errors are even much lower than what was observed for 102 nm size particles. The total scattering error ranges between 0.227 to 0.591% for total scattering and 0.411 to 1.11% for scattering cross-section (Table 7).

The percentage error for 296 nm particles ranges from 2.24 % to 3.26 % for total scattering and from 2.4 to 3.33 % for scattering cross-section (Table 8). These values were much narrower than that of 102 nm particles but the values are a bit higher than what was observed for the 203 nm size particles.

Expt#	WL in nm	Particle/cc	Mie-Xsec	Mie-Total scatter	Experi. Total scatter	Experi. X-sec	%err X-sec	%err Total scatter
1	5.89E-07	278	8.84E-14	2.45E-05	2.40E-05	8.6275E-14	2.40E+00	2.24E+00
2	5.89E-07	287	8.84E-14	2.54E-05	2.47E-05	8.5817E-14	2.92E+00	2.90E+00
3	5.89E-07	283	8.84E-14	2.50E-05	2.42E-05	8.5607E-14	3.16E+00	3.22E+00
4	5.89E-07	274	8.84E-14	2.42E-05	2.35E-05	8.5945E-14	2.78E+00	2.70E+00
5	5.89E-07	275	8.84E-14	2.43E-05	2.35E-05	8.5454E-14	3.33E+00	3.26E+00

**Table 8 Theoretical and experimental total scattering and scattering cross-section for 296 nm polystyrene spheres at 589 nm without the blower**

Expt #	WL in nm	Experi- Total scatter	Partic/cc	Experi x-sec	Mie-Xsec	Mie-Total scatter	%err- x-sec	%err-Total scatter
1	5.89E-07	5.07E-07	1755	2.89E-16	2.24E-16	3.93E-07	2.90E+01	2.91E+01
2	5.89E-07	4.27E-07	1743	2.45E-16	2.24E-16	3.90E-07	9.38E+00	9.49E+00
3	5.89E-07	5.21E-07	1759	2.96E-16	2.24E-16	3.94E-07	3.22E+01	3.22E+01
4	5.89E-07	4.80E-07	1752	2.74E-16	2.24E-16	3.93E-07	2.24E+01	2.23E+01
5	5.89E-07	4.59E-07	1742	2.63E-16	2.24E-16	3.90E-07	1.76E+01	1.76E+01

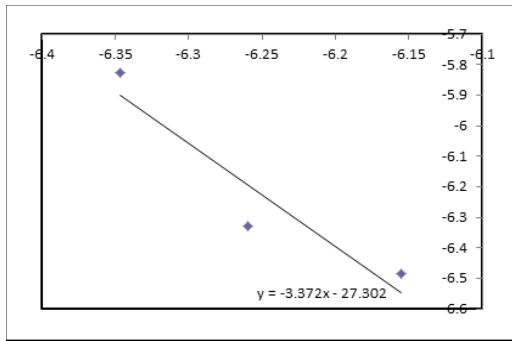
**Table 6 Theoretical and experimental total scattering and scattering cross-section of 102 nm polystyrene spheres at 589 nm without the blower**

Expt#	WL in nm	Particle/cc	Mie-Xsec	Mie-Total scatter	Experi. Total scatter	Experi. x-sec	% Err-Total scatter	%Err- X-sec
1	5.89E-07	660	1.27E-14	8.37E-06	8.4195E-06	1.2757E-14	5.91E-01	4.47E-01
2	5.89E-07	656	1.27E-14	8.32E-06	8.2953E-06	1.2648E-14	2.97E-01	4.11E-01
3	5.89E-07	638	1.27E-14	8.09E-06	8.0944E-06	1.2695E-14	5.45E-02	4.29E-02
4	5.89E-07	626	1.29E-14	7.94E-06	7.9837E-06	1.2759E-14	5.50E-01	1.11E+00
5	5.89E-07	622	1.27E-14	7.89E-06	7.9406E-06	1.2761E-14	6.41E-01	4.82E-01
6	5.89E-07	617	1.26E-14	7.83E-06	7.8122E-06	1.2657E-14	2.27E-01	4.53E-01

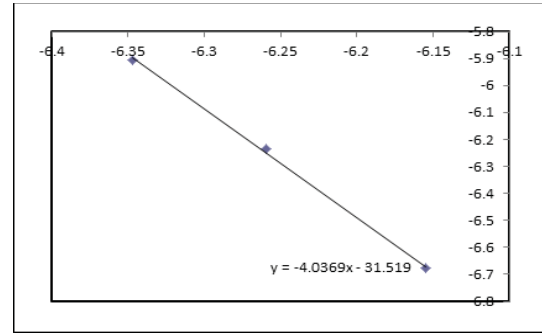
**Table 7 Theoretical and experimental total scattering and scattering cross-section for 203 nm Polystyrene spheres at 589 nm without the blower**

Expt#	WL in nm	Particle/cc	Mie-Xsec	Mie-Total scatter	Experi. Total scatter	Experi. X-sec	%err X-sec	%err Total scatter
1	5.89E-07	278	8.84E-14	2.45E-05	2.40E-05	8.6275E-14	2.40E+00	2.24E+00
2	5.89E-07	287	8.84E-14	2.54E-05	2.47E-05	8.5817E-14	2.92E+00	2.90E+00
3	5.89E-07	283	8.84E-14	2.50E-05	2.42E-05	8.5607E-14	3.16E+00	3.22E+00
4	5.89E-07	274	8.84E-14	2.42E-05	2.35E-05	8.5945E-14	2.78E+00	2.70E+00
5	5.89E-07	275	8.84E-14	2.43E-05	2.35E-05	8.5454E-14	3.33E+00	3.26E+00

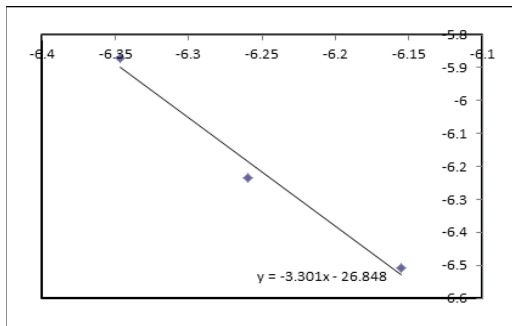
**Table 8 Theoretical and experimental total scattering and scattering cross-section for 296 nm polystyrene spheres at 589 nm without the blower**



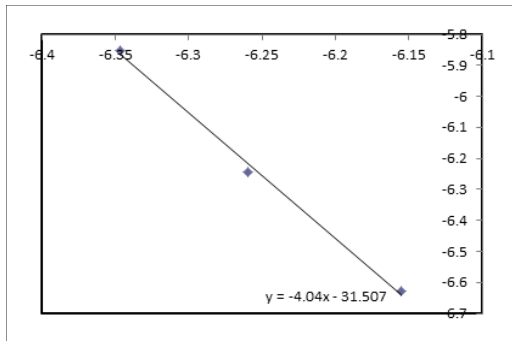
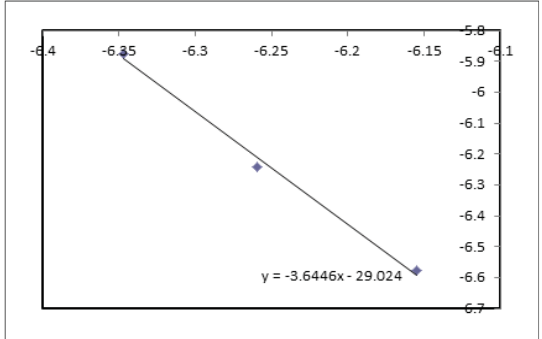
A



B



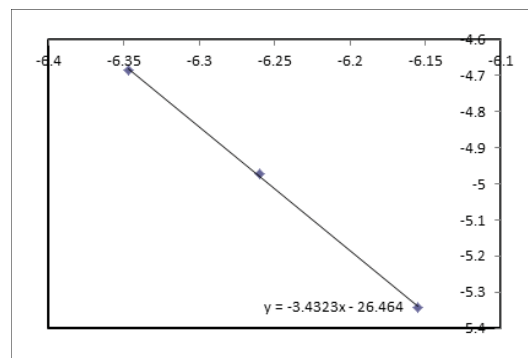
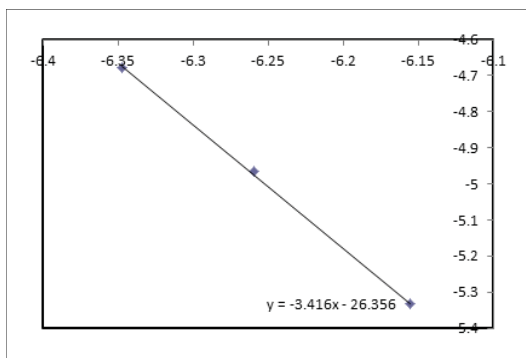
C



E

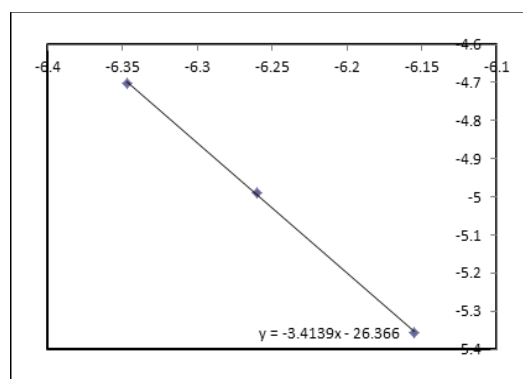
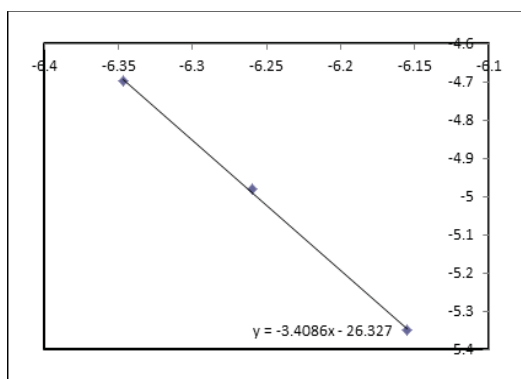
**Figure 6. Scatter plots to estimate the scattering coefficient at 589 nm wavelength, using the scattering coefficient measured at 450, 550 and 700 nm wavelengths for 102 nm size particles without external blower.**





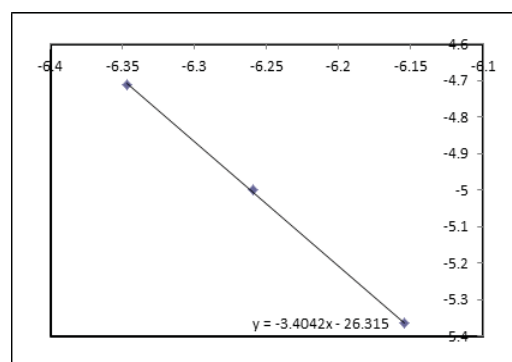
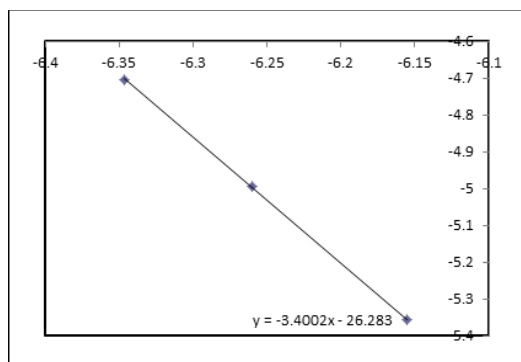
A

B



C

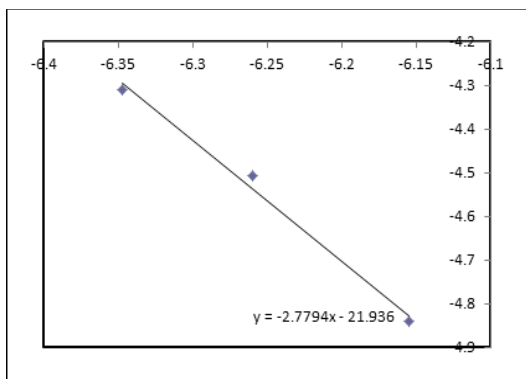
D



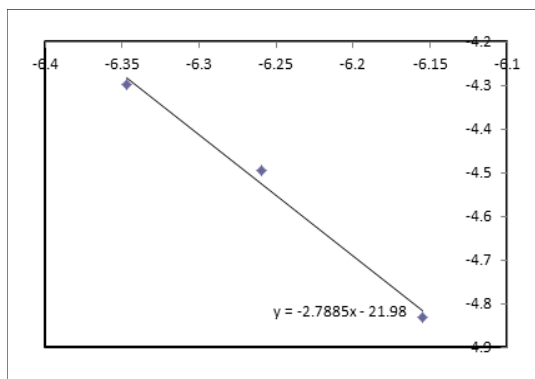
E

F

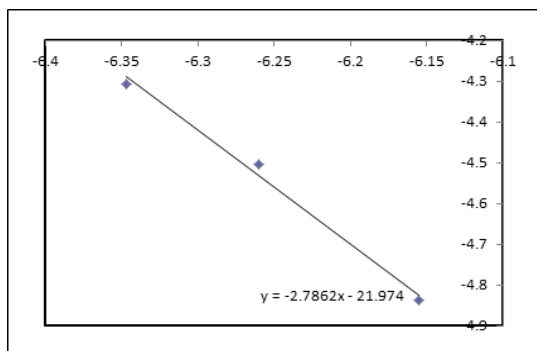
**Figure 7. Scatter plots to estimate the scattering coefficient at 589 nm wavelength, using the scattering coefficient measured at 450, 550 and 700 nm wavelengths for 203 nm size particles without external blower.**



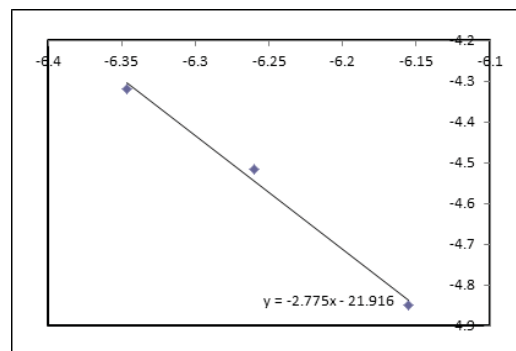
A



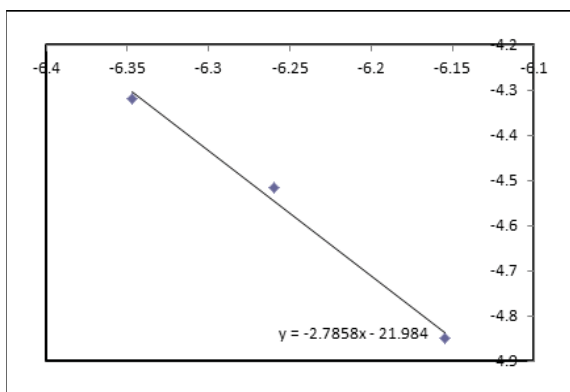
B



C



D



E

**Figure 8. Scatter plots to estimate the scattering coefficient at 589 nm wavelength, using the scattering coefficient measured at 450, 550 and 700 nm wavelengths for 296 nm size particles without external blower.**

#### 4.4 Extinction measurement

In order to quantify the extinction coefficient and extinction cross-section of the polystyrene spheres alone, it is necessary to see effect of water vapor over all measurements. To this end, we have plotted the ring-down spectra of water vapor and that of the polystyrene spheres on the same scale.

The ring-down time spectra to characterize the 102 nm polystyrene spheres indicate a ring down time that coincides with that of the water vapor (Figure 9). Although the ring-down time generally increases in magnitude with wavelength for all the polystyrene spheres that we measure, a low ring-down time is observed at 592nm, 590 nm 595.5 nm and 597 nm wavelengths.

In the case of 203 nm polystyrene spheres, there is a clear difference in the magnitude of the ring-down time between water vapor and when aerosols were introduced in to the cavity (Figure 10). However, there is still a lower ring-down time at similar wavelengths observed for the 102 nm polystyrene spheres spectra. The magnitude of the ring-down time increases with wavelength as in the case of the 102 nm spheres. The water vapor and the polystyrene latex sphere spectra coincide at 592 nm and 597 nm wavelengths. This implies stronger influence of the water vapor absorption at those wavelengths for the 102 nm particles than on the other wavelengths.

Similar to the 102 and 203 nm particles, the ring-down time spectra of the 296 nm particles has an increasing trend with wavelength. The difference in ring-down time

between the water vapor spectra and the six readings when 296 nm aerosol particles were introduced in to the cavity is bigger than what was observed for the 203 nm particles (Figure 11) .The aerosol spectra and the water vapor spectra coincide at 592 nm wavelength.

As the ring-down time spectra alone are not enough to study the extinction behavior of the polystyrene spheres, we determine the extinction coefficient using equation (19). Although not exaggerated as in the case of the ring-down time spectra, at wavelengths where the ring down time was anomalously low, the corresponding extinction coefficient is high in all polystyrene spheres (Figure 12,Figure 13,Figure 14).As further cleaning of those anomalously influenced points is required below we describe results of estimated extinction coefficient after the cleaning process.

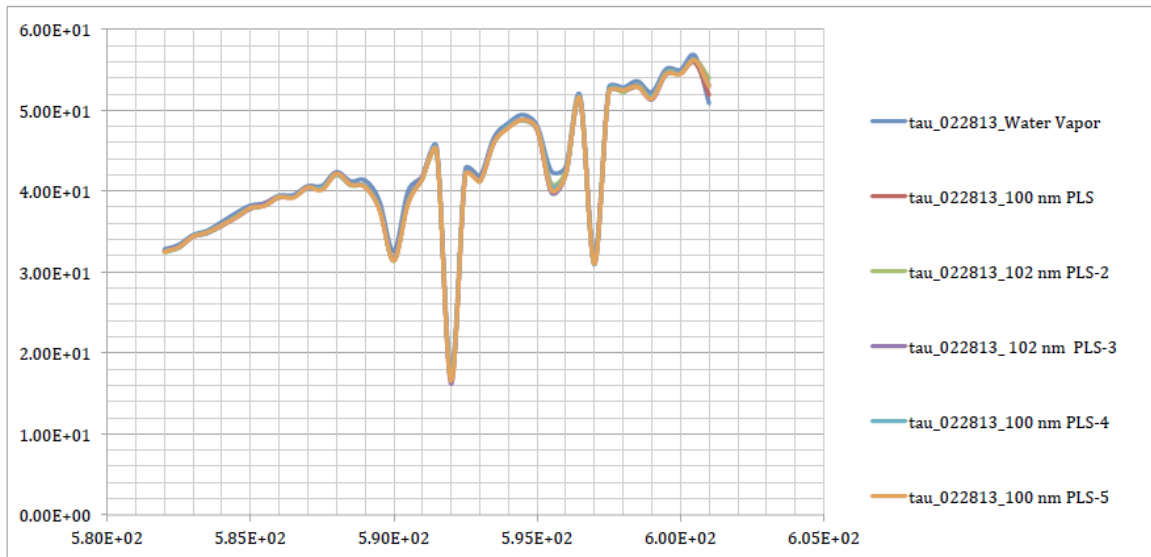


**Figure 9 Ring down time of water vapor and 102 nm Polystyrene latex spheres as a function of wavelength.**

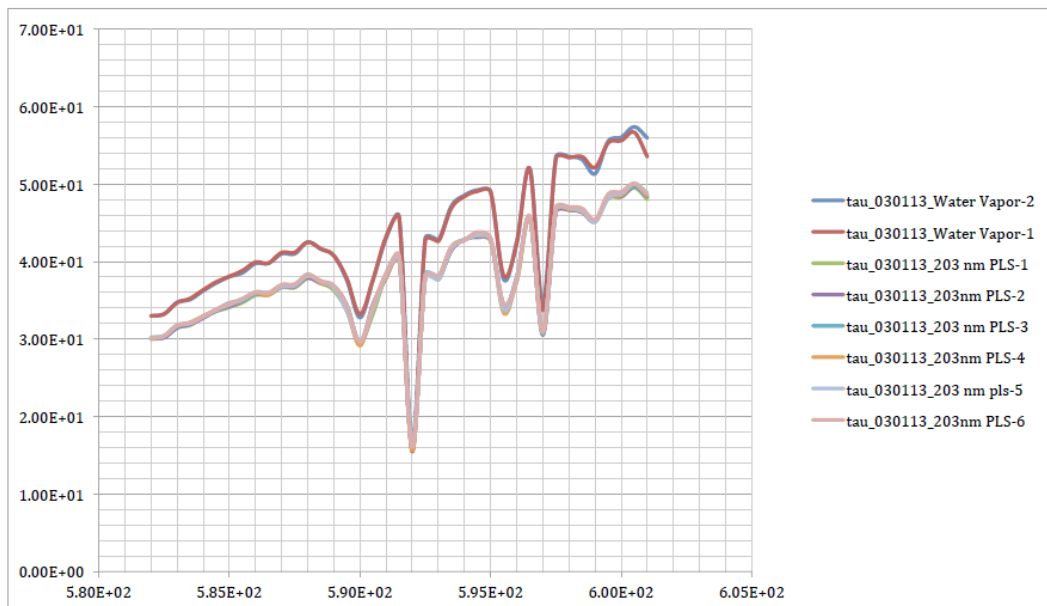


**Figure 10** Ring down time of water vapor and 203 nm Polystyrene latex spheres as a function of wavelength.

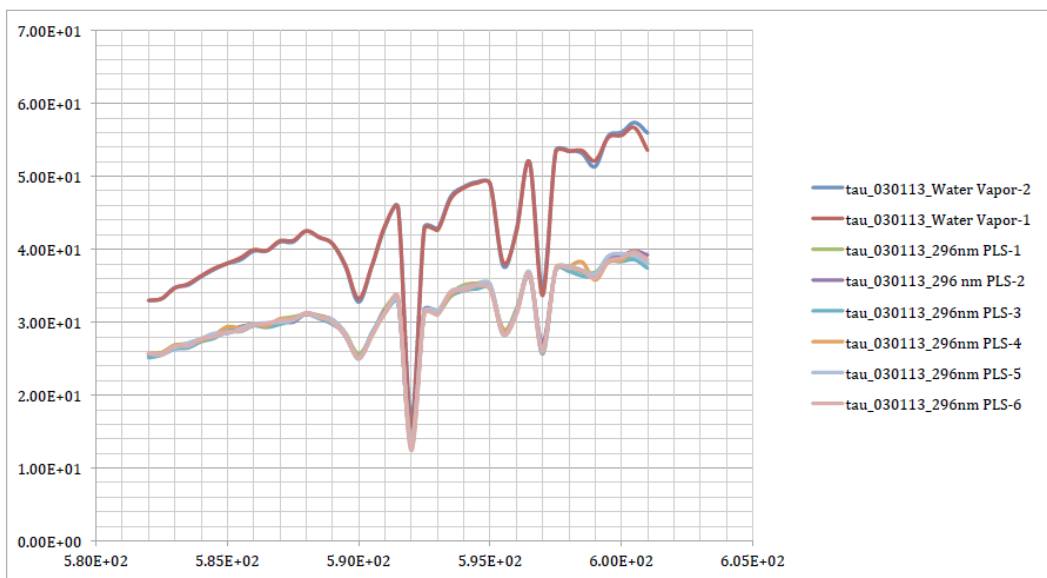


**Figure 11** Ring down time of water vapor and 296 nm Polystyrene latex spheres as a function of wavelength.

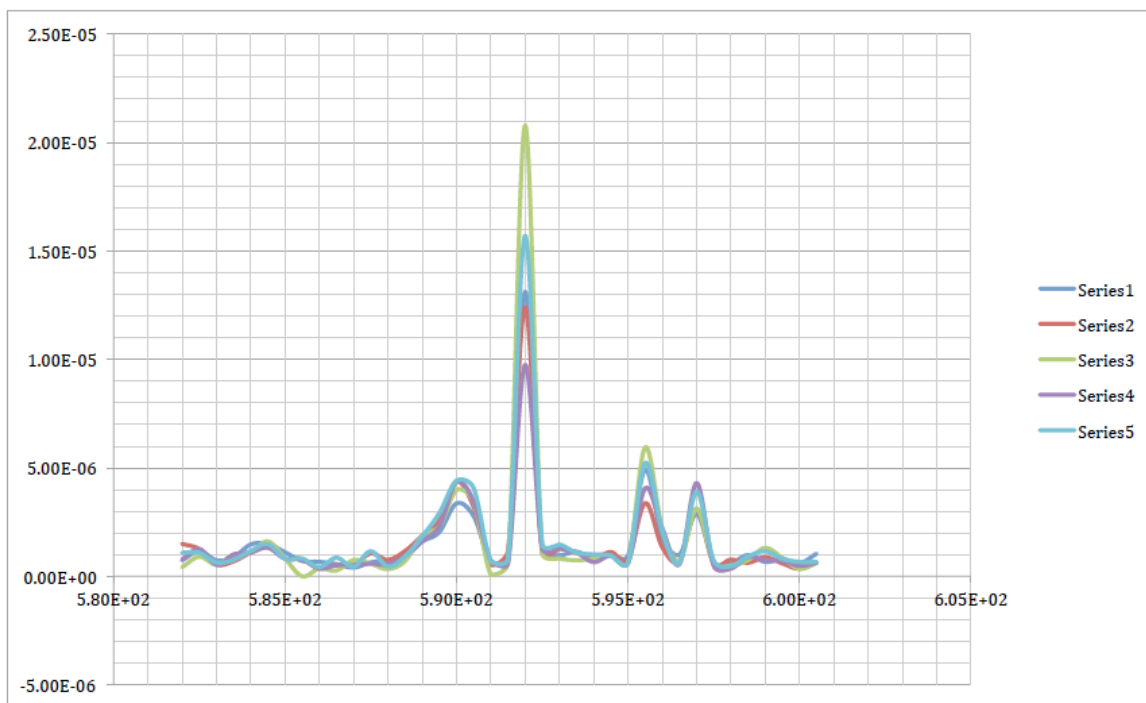


**Figure 12. Extinction coefficient of 103 nm Polystyrene latex spheres using CRD as a function of wavelength in nm**

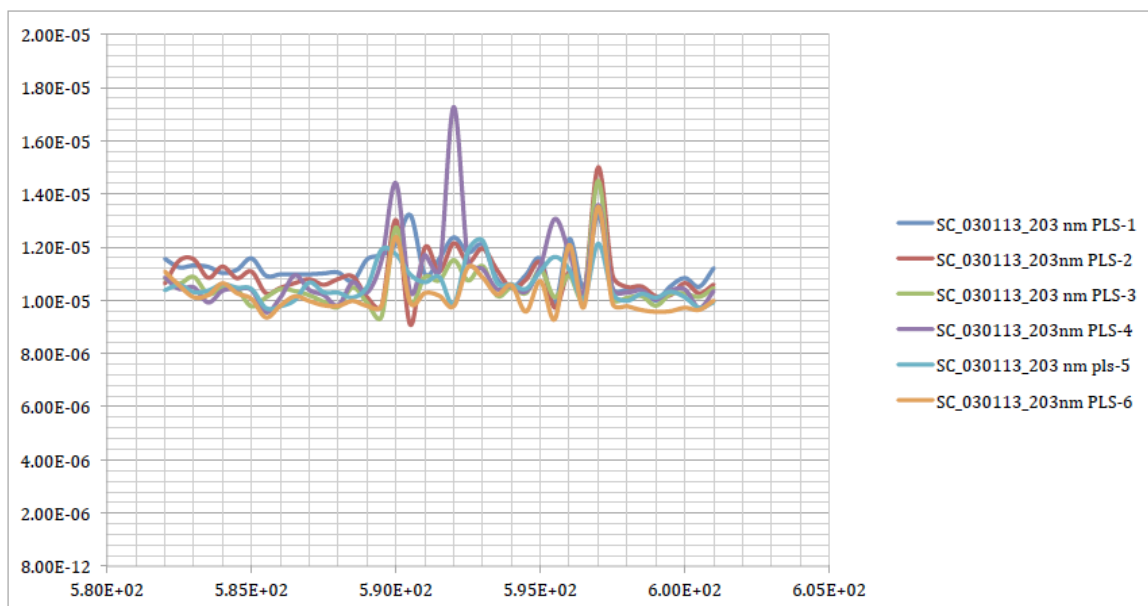


**Figure 13 Extinction coefficient of 203 nm Polystyrene latex spheres using CRD as a function of wavelength in nm**

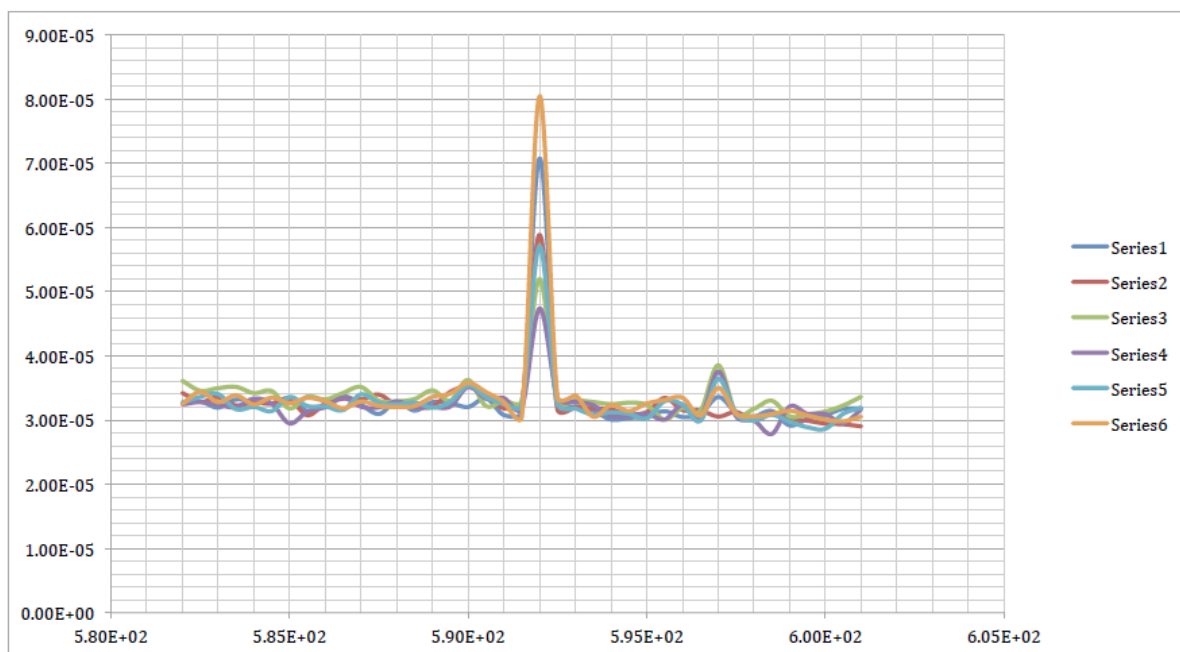


**Figure 14 Extinction coefficient of 296 nm Polystyrene latex spheres using CRD as a function of wavelength in nm**

### **102 nm particles**

To determine the extinction coefficient of the polystyrene aerosols at 589 nm, we removed the water absorption lines. The first and the last points in the spectra were also removed.

The resulting spectra of the 102 nm particles after the water vapor effect has been removed indicate a slight difference but retain an overall similarity (Figure 15, Figure 16, Figure 17, Figure 18, Figure 19). The estimated extinction coefficient ranges from  $4.81 \times 10^{-07}$  to  $7.92 \times 10^{-07}$  with a variance and standard deviations of  $1.59 \times 10^{-14}$  and

$1.26 \times 10^{-07}$  respectively. On the other hand single extinction values at 589nm wavelength taken directly from the spectra vary from  $1.48 \times 10^{-06}$  to  $1.72 \times 10^{-06}$  with variance of  $1.53 \times 10^{-14}$  and standard deviation of  $1.24 \times 10^{-07}$ . The extinction cross-section ranges from  $2.73568 \times 10^{-16}$  to  $4.50992 \times 10^{-16}$  with a standard deviation of  $7.28 \times 10^{-17}$  (Table 9).

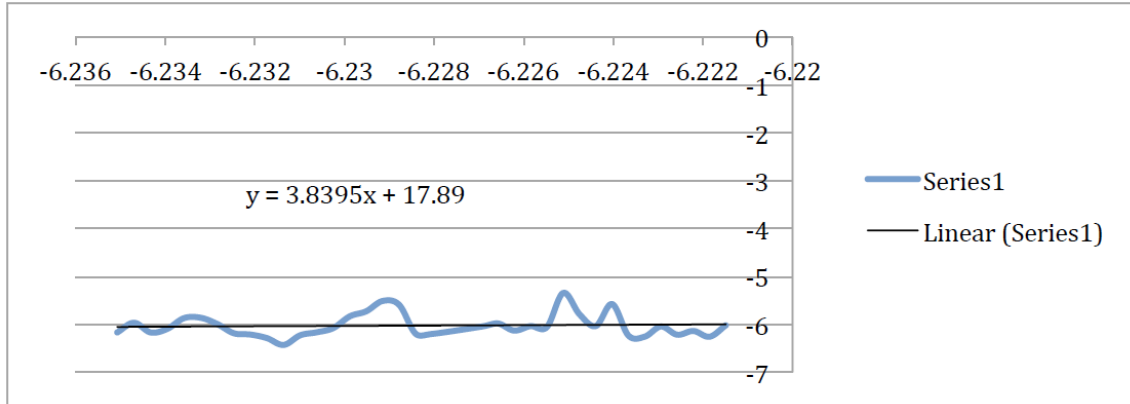


**Figure 15. Spectra of 102 nm polystyrene latex spheres with fitted trend regression line to estimate the extinction coefficient (1st measurement) . X axis is logarithm of the wave length and the y axis is logarithm of extinction coefficient.**

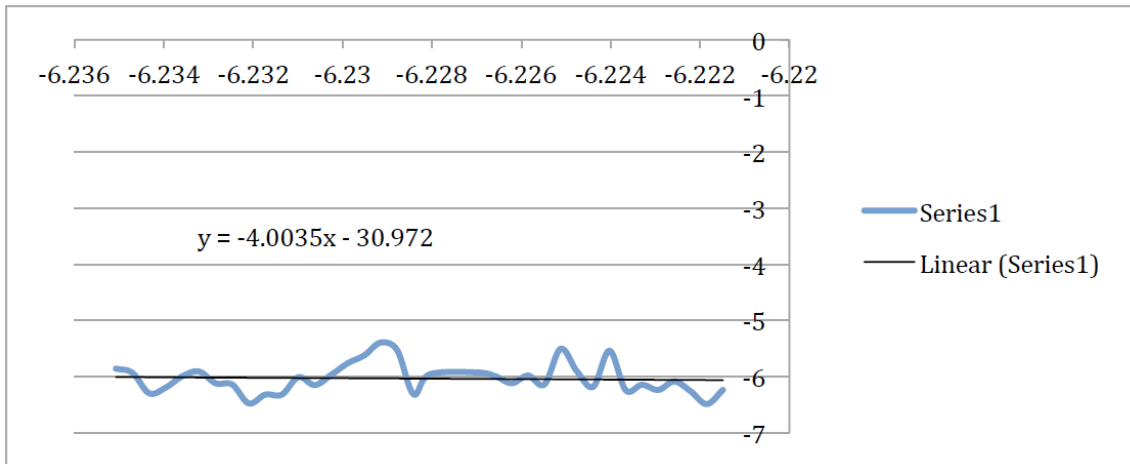


**Figure 16. Spectra of 102 nm polystyrene latex spheres with fitted trend regression line to estimate the extinction coefficient (2nd measurement) . X axis is logarithm of the wave length and the y axis is logarithm of extinction coefficient.**



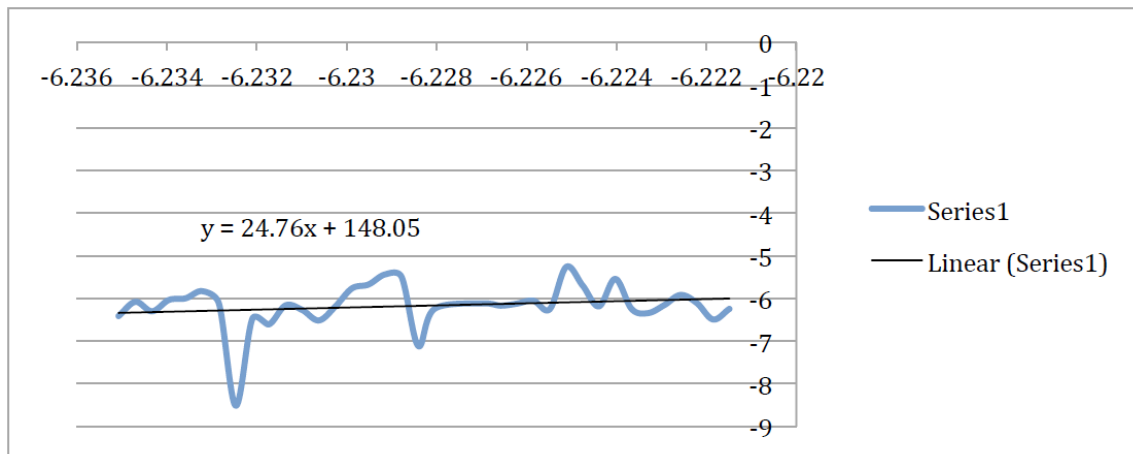


**Figure 17. Spectra of 102 nm polystyrene latex spheres with fitted trend regression line to estimate the extinction coefficient (3rd measurement) . X axis is logarithm of the wave length and the y axis is logarithm of extinction coefficient.**

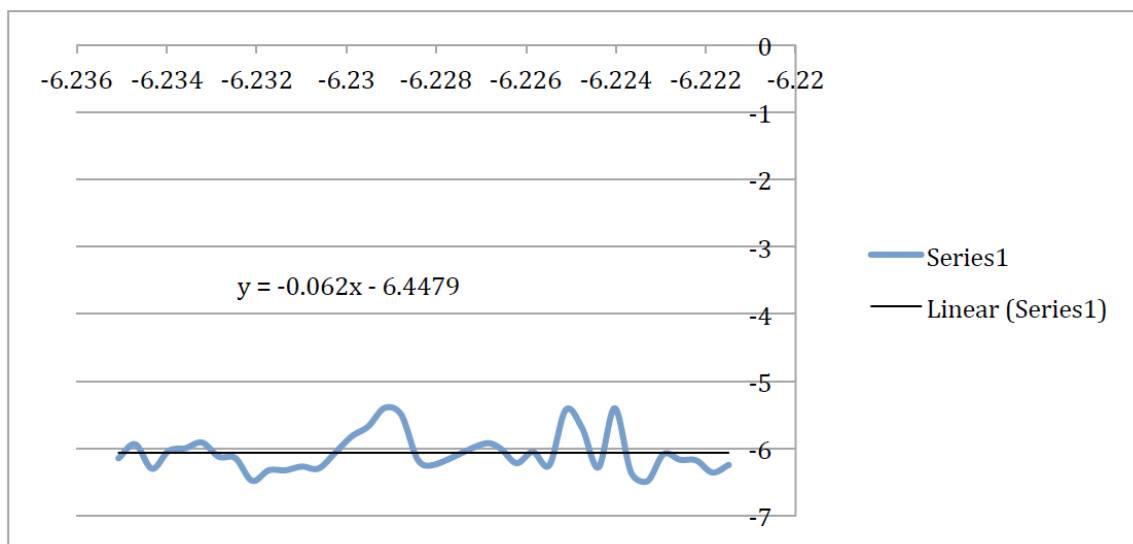


**Figure 18. Spectra of 102 nm polystyrene latex spheres with fitted trend regression line to estimate the extinction coefficient (4th measurement) . X axis is logarithm of the wave length and the y axis is logarithm of extinction coefficient.**

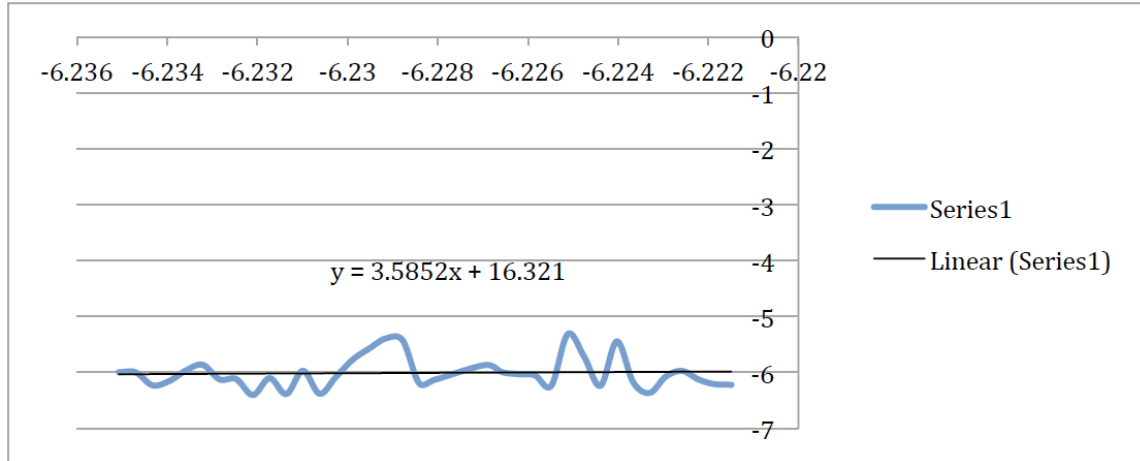


**Figure 19. Spectra of 102 nm polystyrene latex spheres with fitted trend regression line to estimate the extinction coefficient (5th measurement) . X axis is logarithm of the wave length and the y axis is logarithm of extinction coefficient.**

### **203 nm particles,**

The spectra of 203 nm particles for the five measurements look a bit different with an overall trend and magnitude of the extinction coefficient remaining similar (Figure 20, Figure 21, Figure 22, Figure 23, Figure 24 and Figure 25). From the slopes of the lines, we estimated extinction coefficient that ranges from  $9.32 \times 10^{-06}$  to  $1.02 \times 10^{-05}$ . The variance of the five measurements is  $1.19 \times 10^{-13}$  with a standard deviation of  $3.42 \times 10^{-07}$ . Those values indicate that the measurements are pretty close. When we consider the extinction coefficient values obtained directly from the spectra at 589 nm wavelengths, the values range from  $9.04 \times 10^{-6}$  to  $1.07 \times 10^{-05}$ . The variance of the five readings is a bit higher than what is calculated using the trend equation. The extinction cross-section ranges from  $1.5 \times 10^{-14}$  to  $1.55204 \times 10^{-14}$  (Table 9). This range is very narrow with variance of  $4.47 \times 10^{-32}$  and standard deviation of  $2.11 \times 10^{-16}$ .

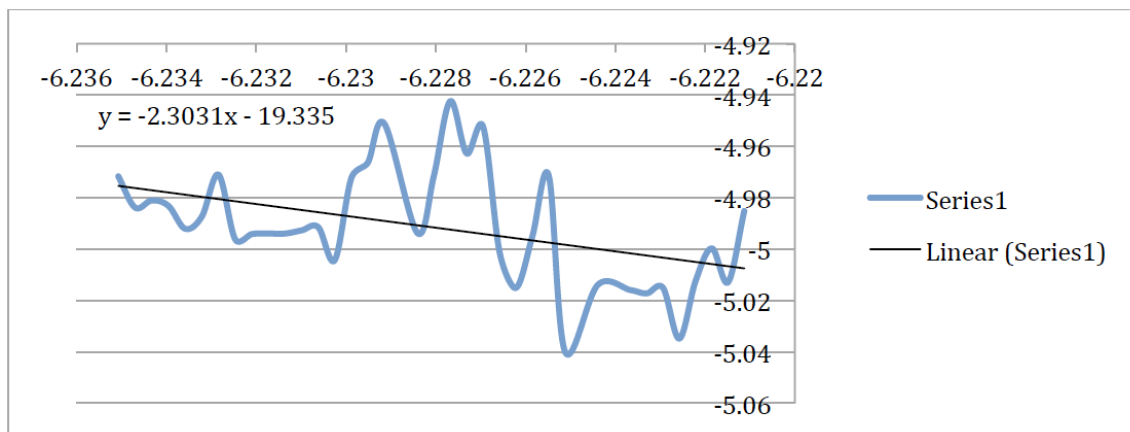


**Figure 20. Spectra of 203 nm polystyrene latex spheres with fitted trend regression line to estimate the extinction coefficient (1st measurement) . X axis is logarithm of the wave length and the y axis is logarithm of extinction coefficient.**

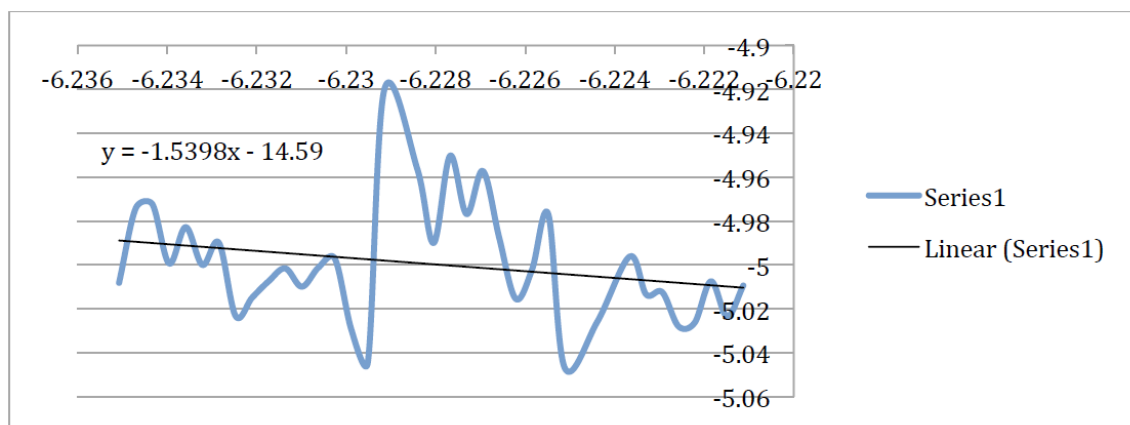


**Figure 21. Spectra of 203 nm polystyrene latex spheres with fitted trend regression line to estimate the extinction coefficient (2nd measurement) . X axis is logarithm of the wave length and the y axis is logarithm of extinction coefficient.**

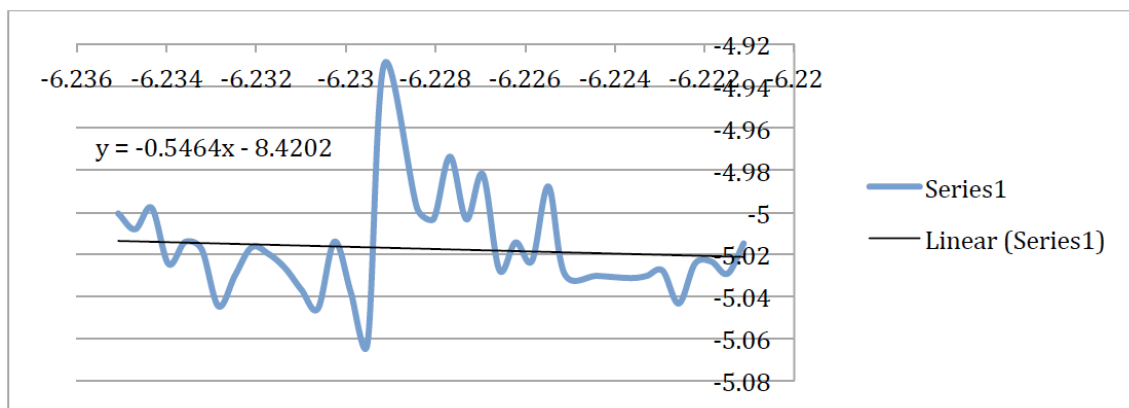


**Figure 22. Spectra of 203 nm polystyrene latex spheres with fitted trend regression line to estimate the extinction coefficient (3rd measurement) . X axis is logarithm of the wave length and the y axis is logarithm of extinction coefficient.**

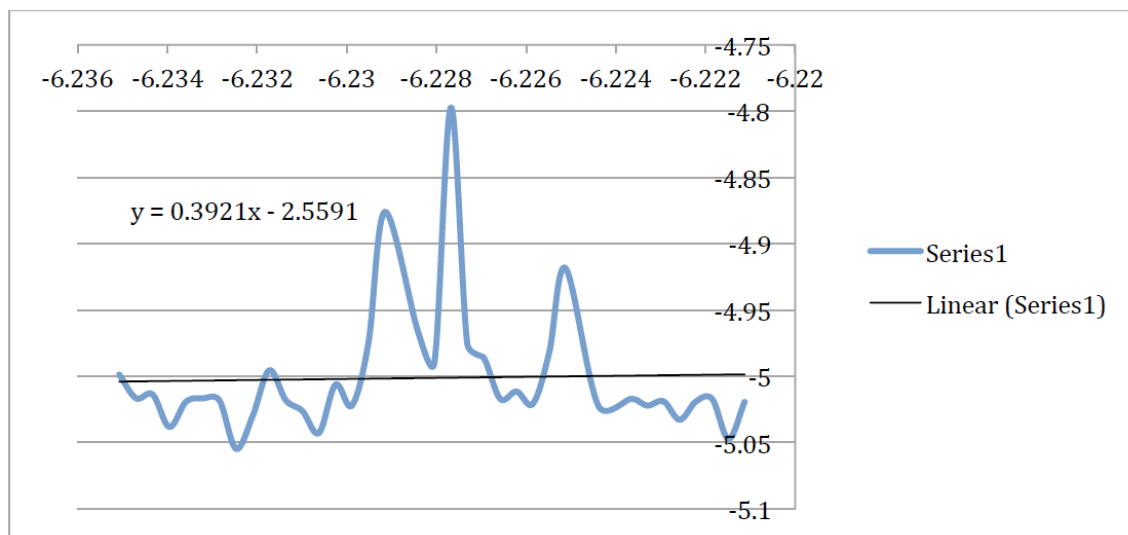


**Figure 23. Spectra of 203 nm polystyrene latex spheres with fitted trend regression line to estimate the extinction coefficient (4th measurement) . X axis is logarithm of the wave length and the y axis is logarithm of extinction coefficient.**

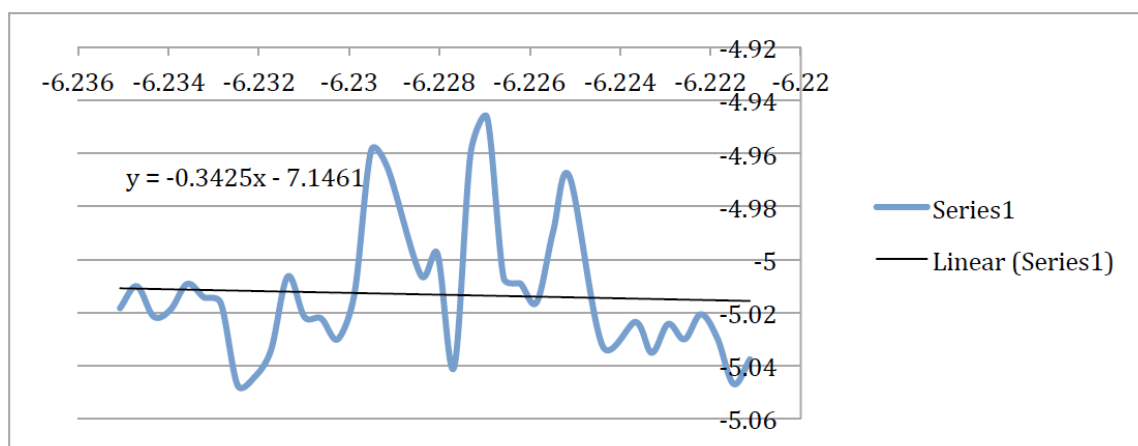


**Figure 24. Spectra of 203 nm polystyrene latex spheres with fitted trend regression line to estimate the extinction coefficient (5th measurement) . X axis is logarithm of the wave length and the y axis is logarithm of extinction coefficient.**

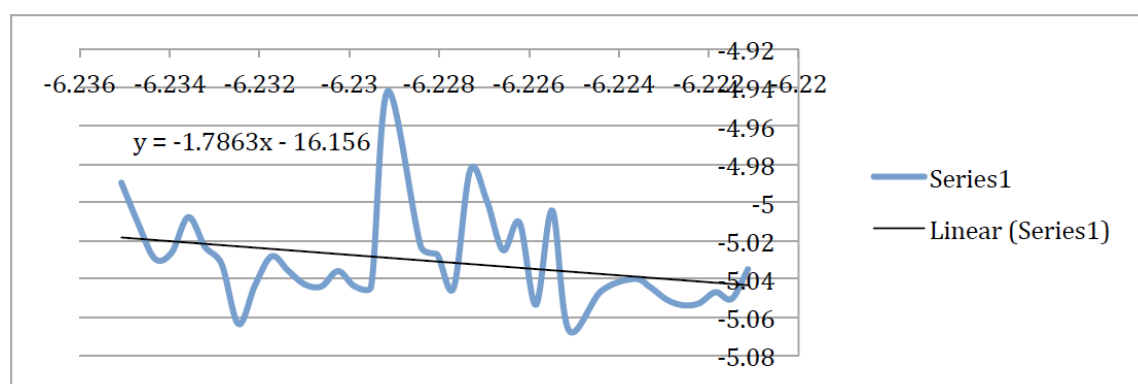


**Figure 25. Spectra of 203 nm polystyrene latex spheres with fitted trend regression line to estimate the extinction coefficient (6th measurement) . X axis is logarithm of the wave length and the y axis is logarithm of extinction coefficient.**

### **296 nm Particles,**

The anomalous extinction coefficient values depicted on the spectra are at 592 nm and 597 nm wavelengths. The remaining part of the spectra have almost similar signature (Figure 26, Figure 27, Figure 28, Figure 29). Extinction coefficient estimated from the regression line ranges from  $2.95 \times 10^{-05}$  to  $3.08 \times 10^{-05}$ . The extinction coefficient values

extracted directly from the spectra on the other hand ranges from  $2.96 \times 10^{-5}$  to  $3.1 \times 10^{-7}$ . The variance and standard deviation of the extinction coefficient estimated using the trend regression equation are  $2.63 \times 10^{-13}$  and  $5.12 \times 10^{-7}$  respectively. The extinction cross-section of 296 nm polystyrene particles, for five measurements, range from  $1.03453 \times 10^{-13}$  to  $1.09142 \times 10^{-13} \text{ (m}^2\text{)}$ (Table 9).

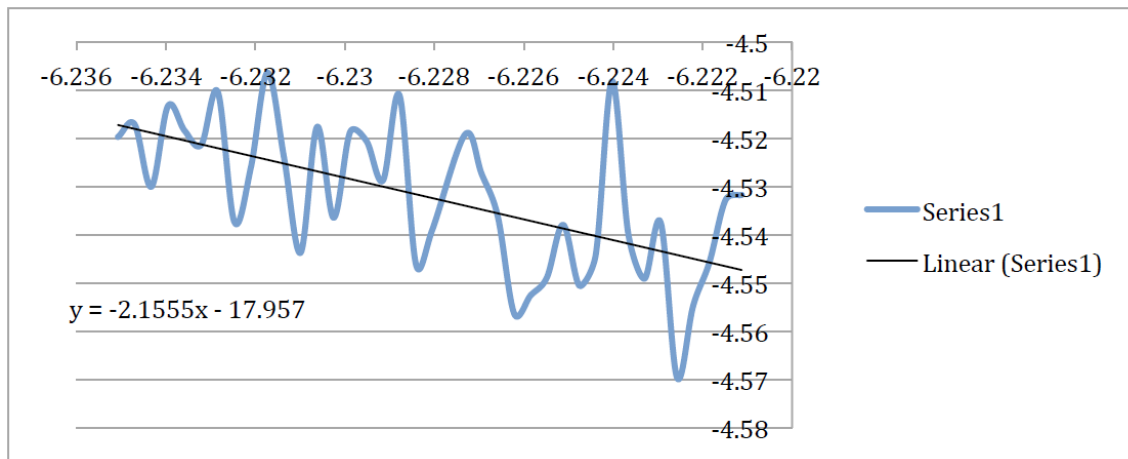


**Figure 26. Spectra of 296 nm polystyrene latex spheres with fitted trend regression line to estimate the extinction coefficient (First measurement) . X axis is logarithm of the wave length and the y axis is logarithm of extinction coefficient.**

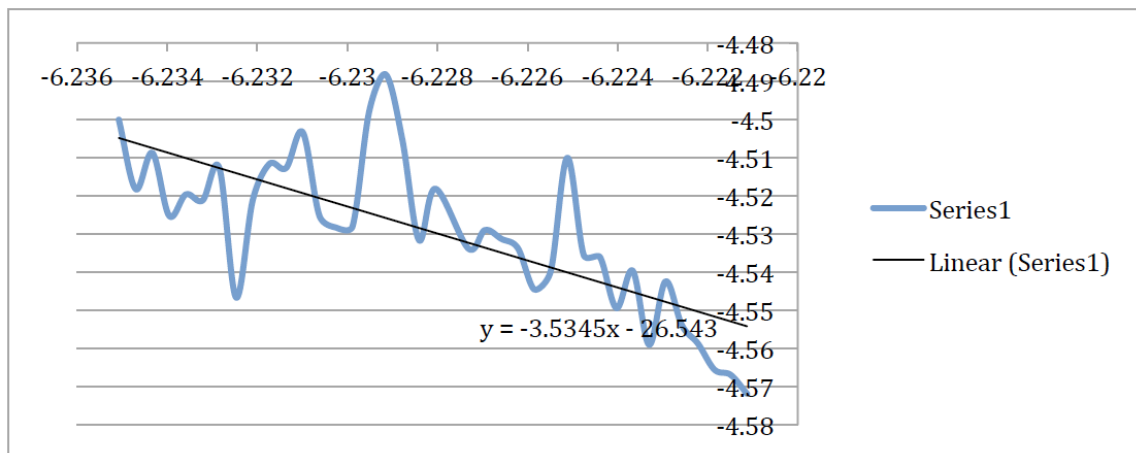


**Figure 27. Spectra of 296 nm polystyrene latex spheres with fitted trend regression line to estimate the extinction coefficient (second measurement) . X axis is logarithm of the wave length and the y axis is logarithm of extinction coefficient.**

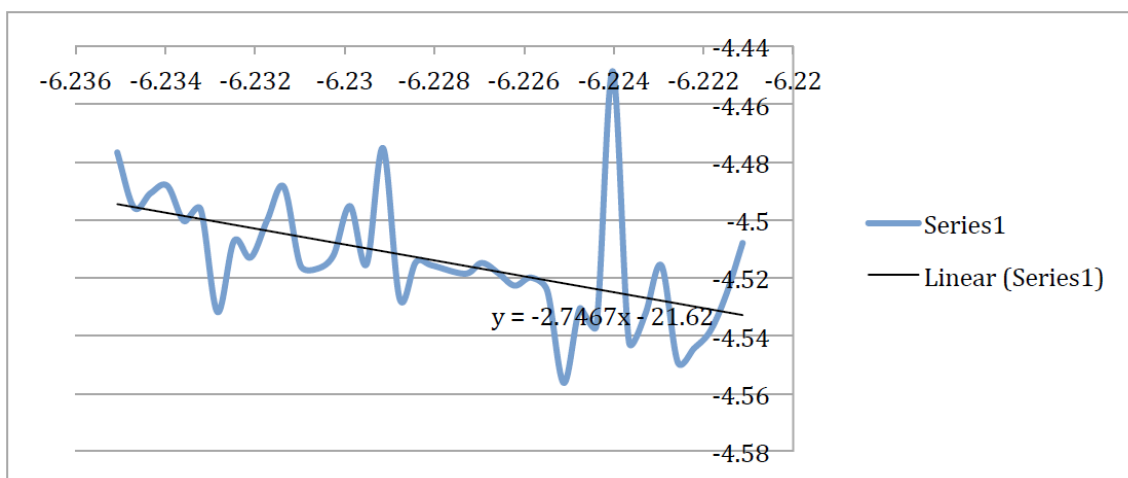


**Figure 27. Spectra of 296 nm polystyrene latex spheres with fitted trend regression line to estimate the extinction coefficient (Third measurement) . X axis is logarithm of the wave length and the y axis is logarithm of extinction coefficient.**

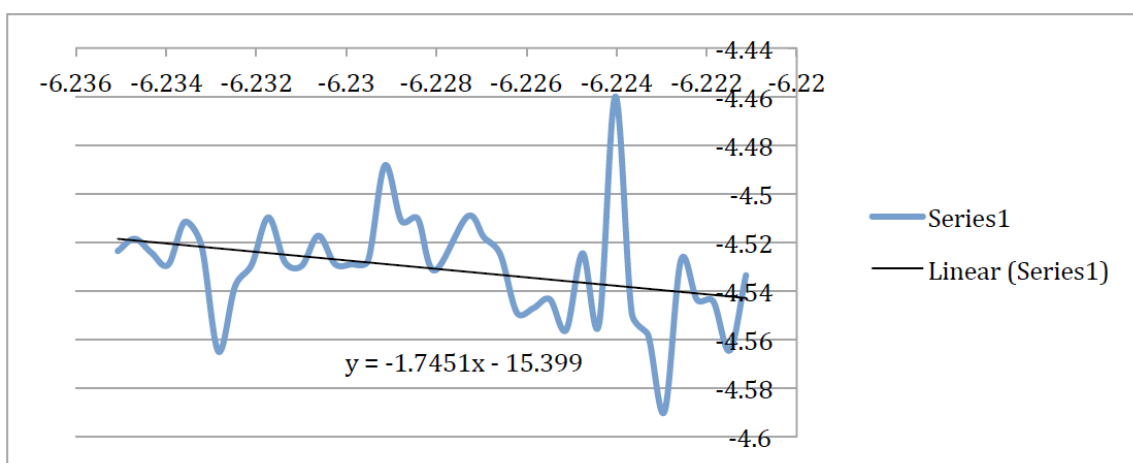


**Figure 28. Spectra of 296 nm polystyrene latex spheres with fitted trend regression line to estimate the extinction coefficient (4th measurement). X axis is logarithm of the wave length and the y axis is logarithm of extinction coefficient.**

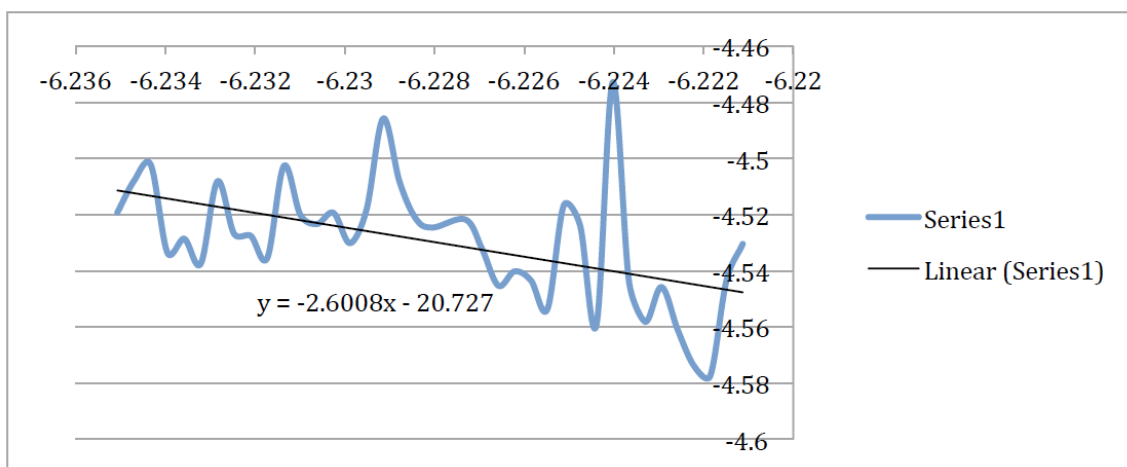


**Figure 28. Spectra of 296 nm polystyrene latex spheres with fitted trend regression line to estimate the extinction coefficient (5th measurement) . X axis is logarithm of the wave length and the y axis is logarithm of extinction coefficient.**

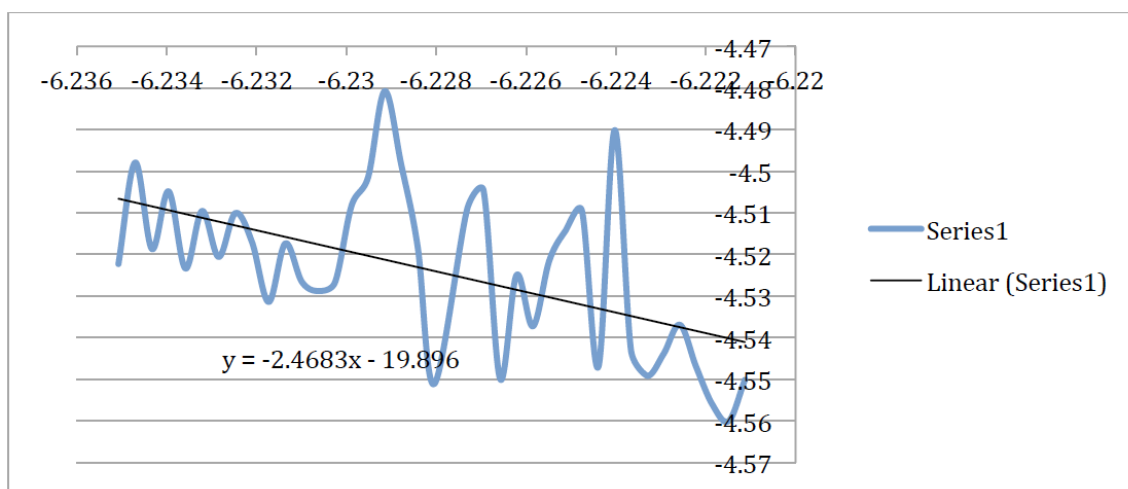


**Figure 29. Spectra of 296 nm polystyrene latex spheres with fitted trend regression line to estimate the extinction coefficient (6th measurement) . X axis is logarithm of the wave length and the y axis is logarithm of extinction coefficient.**

### Single scattering albedo

From the scattering coefficient and extinction measurements we calculated the single scattering albedo for 102, 203 and 296 nm particles. In (Table 9) we have shown



calculated values from the angstrom coefficient based extinction prediction and those from the extracted extinctions at 589 nm taken directly from the spectra. Below we discuss only those obtained from the angstrom coefficient predictions.

The single scattering albedo of the 102 nm polystyrene spheres ranges from 0.567 to 1.08 for the extinction predicted using the angstrom coefficient at 589 nm wavelength (Table 9). While calculated values of the four experiments generally lie between 0.567 and 0.687, one measurement is quite large; higher than a theoretically expected value of 1.

For the 203 nm particles, the single scattering albedo ranges from 0.822 to 0.846 (Table 9). Those values are much better than what is estimated for the 102 nm particles. However those values are off by 18 to 15% from the theoretical value (Table 9).

Single scattering albedo measurement of the 296 nm spheres range from 0.794 to 0.81. Those values are also better than the 102 nm size spheres (Table 9). Nevertheless, they are 19 to 20 % off the theoretically expected value.

296nm							
WL(m)	Extinction (m <sup>-1</sup> )	Extinction spectral value	Particles/cc	Total scattering (m <sup>-1</sup> )	SSA	SSA from spectra value	X-sec (m <sup>2</sup> )
5.89E-07	2.96E-05	3.03E-05	277.623	2.40E-05	8.10E-01	7.91E-01	1.06E-13
5.89E-07	2.97E-05	2.97E-05	287.3833	2.47E-05	8.30E-01	8.32E-01	1.03E-13
5.89E-07	3.08E-05	3.20E-05	282.6155	2.42E-05	7.84E-01	7.57E-01	1.09E-13
5.89E-07	2.95E-05	2.96E-05	273.9733	2.35E-05	7.99E-01	7.96E-01	1.08E-13
5.89E-07	2.96E-05	2.95E-05	275.0938	2.35E-05	7.94E-01	7.97E-01	1.08E-13
<b>Average</b>	<b>2.98E-05</b>	<b>3.02E-05</b>	<b>2.79E+02</b>	<b>2.40E-05</b>	<b>8.03E-01</b>	<b>7.95E-01</b>	<b>1.07E-13</b>
<b>STD</b>	<b>5.12E-07</b>	<b>9.89E-07</b>	<b>5.594725</b>	<b>4.80E-07</b>	<b>0.017282</b>	<b>0.026641</b>	<b>2.12E-15</b>
102nm							
5.89E-07	7.92E-07	1.48E-06	1755.233	5.07E-07	6.40E-01	3.44E-01	4.51E-16
5.89E-07	7.53E-07	1.73E-06	1742.787	4.27E-07	5.67E-01	2.47E-01	4.32E-16
5.89E-07	4.81E-07	1.73E-06	1759.218	5.21E-07	1.08E+00	3.02E-01	2.74E-16
5.89E-07	6.99E-07	1.51E-06	1752.163	4.80E-07	6.87E-01	3.17E-01	3.99E-16
5.89E-07	7.66E-07	1.70E-06	1741.944	4.59E-07	5.99E-01	2.70E-01	4.40E-16
<b>Average</b>	<b>6.98E-07</b>	<b>1.63E-06</b>	<b>1.75E+03</b>	<b>4.79E-07</b>	<b>7.15E-01</b>	<b>2.96E-01</b>	<b>3.99E-16</b>
<b>STD</b>	<b>1.26E-07</b>	<b>1.24E-07</b>	<b>7.64E+00</b>	<b>3.76E-08</b>	<b>2.10E-01</b>	<b>3.81E-02</b>	<b>7.28E-17</b>
203nm							
5.89E-07	1.02E-05	1.07E-05	659.9912	8.42E-06	8.22E-01	7.90E-01	1.55E-14
5.89E-07	1.01E-05	9.34E-06	655.8564	8.30E-06	8.24E-01	8.88E-01	1.53E-14
5.89E-07	9.57E-06	9.15E-06	637.6285	8.09E-06	8.46E-01	8.84E-01	1.50E-14
5.89E-07	9.64E-06	9.51E-06	625.7429	7.98E-06	8.29E-01	8.40E-01	1.54E-14
5.89E-07	9.63E-06	9.71E-06	622.2338	7.94E-06	8.25E-01	8.18E-01	1.55E-14
5.89E-07	9.32E-06	9.04E-06	617.2047	7.81E-06	8.39E-01	8.64E-01	1.51E-14
<b>Average</b>	<b>9.74E-06</b>	<b>9.58E-06</b>	<b>6.36E+02</b>	<b>8.09E-06</b>	<b>8.31E-01</b>	<b>8.47E-01</b>	<b>1.53E-14</b>
<b>STD</b>	<b>3.44E-07</b>	<b>5.84E-07</b>	<b>1.80E+01</b>	<b>2.29E-07</b>	<b>9.65E-03</b>	<b>3.86E-02</b>	<b>2.11E-16</b>

**Table 9** extinction coefficient, single scattering albedo and extinction cross-section of 296, 102 and 203 nm particles.

## CHAPTER 5- DISCUSSION

### 5.1. Comparison with Mie theory calculations

Published nephelometer uncertainty values are generally up to 10%. Considering this uncertainty, the overall accuracy of our measurement is higher for the 203 and 296 nm spheres and considerably low for the 102 nm polystyrene spheres. Several possible sources of uncertainty are indicated in chapter 2. Below we discuss our measurement errors with respect to the possible source.

The effect of particles loss on optical property measurements could be high depending on the magnitude of loss and on the wavelength at which the measurement is done. Calculated total scattering coefficient from a Mie predicted scattering cross section and the number of particles lost within the measurement volume are significant for the 102 nm polystyrene spheres than the 296 nm polystyrene spheres.

As corrections need to be done on the raw data, we calculated the scattering coefficient due particles loss using Mie theory calculations. The estimated total scattering coefficient values, due to loss, for the 102 nm size polystyrene particles accounts to about  $1.319 \times 10^{-7}$ ,  $3.490 \times 10^{-7}$ ,  $7.805 \times 10^{-7} \text{ m}^{-1}$  at 700, 550 and 450 nm wavelength respectively when an external blower was fitted to the nephelometer (for  $1182 \text{ particles/cm}^3$ ). Without the external blower a total scattering reduction of  $3.150 \times 10^{-7}$ ,  $1.408 \times 10^{-7}$ , and  $5.324 \times 10^{-8} \text{ m}^{-1}$  are measured at 450, 550 and 700 nm wavelength (i.e. for a loss of  $477 \text{ particles/cm}^3$ ). Similarly a total scattering reduction of about  $5.483 \times 10^{-6}$ ,  $3.62 \times 10^{-6}$ , and  $1.637 \times 10^{-6}$  is

possible when an external blower is fitted to the nephelometer at 450, 550 and 700 nm wavelength for the 296 nm size particles (32 particles/cc). Without the external blower,  $1.228 \times 10^{-6}$ ,  $2.715 \times 10^{-6}$  and  $4.113 \times 10^{-6} \text{ m}^{-1}$  reduction in scattering coefficient at 700, 550 and 450 nm wavelength is possible for the 296 nm size polystyrene spheres without an external blower (24 particles/cc). The above corrections will be applicable when the scattering effects of the particles are not counted by the nephelometer. However, if the particle loss was detected after the measuring volume i.e if their contribution is already included in the scattering measurement, the possible particle loss correction would be on the final scattering cross-section measurement.

The above values are theoretically predicted loss generated errors. The observed uncertainties however range from 17.6 to 32.23 % for the 102 nm spheres and 2.24 to 3.26 for the 296 nm polystyrene spheres. This implies that, besides the error introduced due to particle loss, there could be other possible sources of errors that contribute to the errors.

Our nephelometer is fairly new instrument with no problems due to accumulation of dirt, contamination, damage, or other physical problems with in the nephelometer or its mounting system. Therefore we assume zero measurement error contributed due to those causes. Below we focus on other possible sources of error, discussed in chapter 2, with respect to our estimations.

## 5.2. Calibration gas uncertainty

One possible source of error is uncertainty that might be introduced when calibrating the nephelometer using calibration gases. For a difference of 4 K between the inlet and outlet temperature of the nephelometer, relative uncertainty in the scattering coefficient of the calibrating gas ( $\sigma_k$ ) could reach about 0.42% for air and 0.95% for CO<sub>2</sub> [33].

If such source of error occurred when we calibrate the nephelometer, a systematic error could have been introduced in all our measurements. As the error uncertainty of the 203 nm is within 0.4 %, this source of error, if it exists, should be insignificant.

## 5.3. Effects of water vapor

Assuming 1031.2 mb pressure and 30% RH would change scattering coefficient of air ( $\sigma_{k\text{-air}}$ ) by  $-0.39\% \pm 0.06\%$  compared to dry air, while a RH of 85% would change  $\sigma_{k\text{-air}}$  by  $-1.1\% \pm 0.2\%$  [33]. As calibration is done with dry air and zeroing was performed with ambient air, water vapor errors introduced during calibration should be negligible. The relative humidity of the nephelometer during scattering measurement for polystyrene spheres was mainly below 28%. However it sometimes reached 48% percent for the 102 nm polystyrene spheres. Therefore the maximum uncertainty due to the increment in relative humidity, if it affects our measurement, would be 0.39%.

#### **5.4. Photon counting uncertainty**

Photon counting uncertainty error contribution depends on the counting scale, gate width and the averaging time. The first two parameters are considered during the design of the instrument. We reduced possible uncertainty, which might arise during averaging, by taking a reasonable averaging time (120 s). Therefore such source of error should be negligible in our measurement.

#### **5.5. Nephelometer angular non-ideality**

The dominant nephelometer non-ideality is the forward scattering truncation from  $0^\circ$  to approximately  $7^\circ$ . This source of error ranges from a few to 10% for sub micrometer particles but could reach (20%-50%) for coarse mode (super micrometer) particles. The polystyrene spheres used in the calibration process are within the sub micrometer particle range. Therefore up to 10% error was expected due to truncation error. If this was the only cause of uncertainty, we would have expected a larger source of error on the 296 nm particles than on the 102 nm spheres. Considering observed uncertainties of <1% for the 203 nm spheres and ~2.6% for the 296 spheres, it is possible to point out that these error source is not a severe problem for the system.

To be able to check the effect of this source of error however, we attempted to correct the scattering coefficient of the 102 and 296 nm size particles using the procedure that involves a linear relationship between a correction factor and the angstrom coefficient [33].

This approach however resulted in a bigger correction factor that leads to over estimation of the scattering coefficient. That may imply, wavelength non-ideality error could be relatively higher for those particles than the effect of truncation angle. On the other hand, the correction constants used may apply for particles having a refractive index slightly lower than the refractive index of the polystyrene spheres,  $m=1.59+0i$ , that we are studying.

The Angstrom coefficient (AC) for the 102 nm particles ranges from 3.32 to 4.05. For the 203 nm particles, the AC values are pretty close ranging from 3.4 to 3.43 and for the 296 nm particles the AC is more or less constant of 2.77. As it can be seen from Figure 4 of [31], the correction factor is between 1 and 1.02 for these angstrom coefficient values. These values are consistent with the low percentage error of our nephelometer measurement. Detailed discussion on the effect of angular and wavelength non idealities in estimating the correction factor is also available on [36] .

## **5.6 Uncertainty in extinction measurements**

The polystyrene spheres used to calibrate the CRD system have a zero imaginary part of their refractive index. This implies that expected absorption coefficient would be zero. Nevertheless, the difference between the extinction coefficient measured by the cavity and the scattering coefficient measured by the nephelometer is different from zero. As the uncertainty in nephelometer measurements are low for the 203 and 296 nm sized particles, we investigated the possible source of error within the CRD measurement.

Length of the cavity,  $L$ , can be measured accurately and the value of the speed of light is well known and hence could not be sources of error. Hence variables that could introduce uncertainty into the extinction measurement could be  $\tau$ ,  $\tau_0$ , and a propagated uncertainty introduced during estimating length of the cavity filled with a sample. Apart from this, particle loss within the cavity, if significant, can also cause additional uncertainty.

Change in the empty-cavity ring down time could be caused due to change in mirror reflectivity, for instance due to deposition of particles on the mirror surface. Although difficult to quantify the error uncertainty due to these effects, we cleaned the mirrors regularly and we measure the empty-cavity ring down time using a time series mode, to identify and correct for any drift in the value of  $\tau_0$ . Therefore, this source of error cannot be significant in our measurements.

The accuracy of the values of  $\tau$  and  $\tau_0$  can also be affected by the presence of higher-order modes. Besides, ignoring the tail end of the ring down decay where data collection was limited by bit noise can also cause measurement uncertainties. For example a 2% change in  $\tau$  for 404 nm particles resulted changes in the experimentally measured  $Q_{\text{ext}}$  values of  $-1.6\%$  and  $+2.4\%$  for the increase and the decrease in the ring down time, respectively [34]. To minimize this source, we run the time series mode several times until the ring down time gets stable before we do the wavelength scanning. We also avoid regions of low signal-to-noise ratio in the ring down trace. Therefore, such uncertainty in the ring down time could not to be that significant to severely affect our estimated  $Q_{\text{ext}}$ .



Another possible source of error could be presence of water residual within the cavity. To minimize or avoid this source of error, the particles went through diffusion dryer before they get in to the cavity. Therefore contribution of this source of error couldn't be that significant to severely affect the extinction measurement. Furthermore, the absorption coefficient of water at  $\lambda = 589 \text{ nm}$  is about  $0.2 \text{ m}^{-1}$ .

Errors may arise from uncertainty in particle number density. A  $\pm 10\%$  uncertainty in the CPC count deemed the true extinction coefficient values, by 0.9 (to simulate a 10% over count by the CPC) and 1.1 (to simulate a 10% undercount by the CPC) [34]. The significance of this source of error should be very small in our system. Had such counting uncertainty existed within our CPC, the effect would have been observed on the nephelometer measurements as well.

The ratios of cavity length to aerosol sample length published in the literature to date vary from 1.13 [37, 38] to 1.67 [34, 39, 40], the uncertainty introduced by this parameter will vary between instruments. The ratio of the cavity length to the distance between the inlet and outlet of the cavity of our system is 1.14. However, experimentally determined cavity length to aerosol sample ratio is 1.053. This is lower than most published values.

Careful measurement of the length filled by the cavity is very crucial to achieve a high precision optical property measurement using the CRD. For instance, if the length of the cavity occupied by aerosol was assumed to be 79 cm, there is a 14.5% increase in the experimentally retrieved value of the extinction efficiency for 404 nm diameter particles

compared with when a value of 90 cm was assumed ( $Q_{\text{ext}} = 3.616$  for  $l = 79$  cm compared with  $Q_{\text{ext}} = 3.158$  for  $l = 90$  cm)[34]. This source of uncertainty is significant and must be corrected before the error propagates to further optical property calculations.

Uncertainty due to multiply charged particles may also affect optical property measurements. For instance, experimentally measured scattering cross-sections for ammonium sulfate found to be 17–47% higher than those predicted by Mie theory[39, 40], and those for polystyrene beads being 2–12% higher [40]. We are not certain about these sources of error and need to be studied. Even though we use a high quality DMA, it is possible that minor errors could have been caused due to this source of error.

Errors could also be introduced due to change in particle morphology. If the drying process creates a thin layer of film on top of the polystyrene spheres, the particles are no more homogenous. Such effect could lead to a false interpretation when nephelometer as well as the CRD measurement is compared with Mie theory calculations that assumes homogenous and perfect spherical particles. We have not tested this effect on our measurement. Therefore it is important to know the change in morphology of the particles inside the cavity. For instance, error could be introduced due to surfactant and adsorbed water on the surface of the polystyrene spheres. A several nanometer-thick layer of residual water or surfactant used to stabilize the particles in solution is likely to be left on the particle surface in the drying process [34]. This may increase the geometrical cross-section of the polystyrene spheres leading to measurement errors in the optical property of the particles.

Particle loss within the cavity was pretty low for the 296 nm particles. The 10 % loss for the 102 nm particles could be significant and must be corrected.

## **5.7 Uncertainty in single scattering albedo**

The imaginary part of the refractive index of the polystyrene spheres is zero. Therefore the expected single scattering albedo would be 1. In other words, the absorption coefficient of the polystyrene spheres would be zero leading to equal values of the extinction coefficient and the scattering coefficient.

As it has been discussed in the earlier sections, the uncertainty in scattering measurements across the nephelometer is below 3% for the 296 polystyrene spheres and below 0.5% for the 203 nm polystyrene spheres. This implies that the largest uncertainty in the single-scattering albedo should be contributed from the uncertainty in extinction measurement for the 203 and 296 nm particles.

For the case of the 102 nm polystyrene spheres, uncertainty of the scattering measurement is not low. This implies that, even though the biggest contribution could be from the extinction measurement, a significant contribution to the error budget is also expected from the scattering measurements as well.

## **CHAPTER 6 –CONCLUSION AND RECOMMENDATIONS**

Comparison of nephelometer scattering coefficient and scattering cross-section measurements with the Mie theory predicted values indicated a good agreement for the 203 and 296 nm polystyrene spheres (<3%). Nevertheless, experimentally measured and theoretically predicted optical properties of the 102 nm polystyrene spheres disagree from 9- 32%.

Experimental results of the extinction coefficient measurement for the 203 and 296 nm polystyrene spheres are higher than the total scattering measurement. This implies that there is absorption involved in the extinction measurement. As these particles are perfectly scattering particles with zero imaginary part of the refractive index, the source of the difference is uncertain. However, possible sources of errors are detailed in the discussion section. Calculated single scattering albedo values are more than 0.8, which is a typical value for most highly scattering aerosols. As the scattering measurements for the 203 and 296 nm polystyrene spheres are done with less uncertainty, the likely source of error in the single-scattering albedo could be a contribution from the uncertainty in the extinction measurements.

For the 102 nm spheres, the uncertainty in single scattering albedo is bigger than that of the 203 and 296 nm particles. As the scattering and extinction coefficient measurement

of the 102 nm spheres was prone to errors, the uncertainty in single scattering albedo could be contributed from both scattering and extinction measurements.

The percent error of our total scattering measurements is below 1 and 3% for the 203 and 296 nm polystyrene particles respectively. This measurement uncertainty is quite good when compared to the literature uncertainty values of up to 7%. This implies that the nephelometer is well calibrated and configured to conduct scattering coefficient of similar sized scattering aerosols.

Loss correction must be accounted when the nephelometer is used with or without an external blower depending on the convenience of respective experiment. Although our values could be taken as correction factors for the TSI nephelometer and our CRD when used to measure optical properties of aerosol particles with similar index of refraction and size with that of polystyrene spheres, we recommend intensive loss measurements for other types of aerosol particles before drawing a conclusive remark.

To increase accuracy of measurement we discussed all the possible source of errors for the scattering and extinction measurements and we recommend further study on the effects of multiply charged particles, surfactant effect, and the effect of uncertainty in the CPC readings.

## BIBLIOGRAPHY

1. H.-m. Hsu, C.-Y.L., A. Guenther, J. J. Tribbia, and S. C. Liu, *Air-chemistry "turbulence": power-law scaling and statistical regularity*. Atmos. Chem. Phys. Discuss., 2011. **11**: p. 9635-9672.
2. Lipfert, F.W., *Air Pollution and Human Health: Perspectives for the '90s and Beyond*. Risk Analysis, 1997. **17**(2).
3. Lake, U.o.H.-C. *The History of Air Quality*. 2013 [cited 2013 April 15]; Available from: <http://prtl.uhcl.edu/portal/page/portal/EIH/archives/outreach/tfors/history>.
4. Markus Jöller, T.B., Ingwald Obernberger, *Modeling of aerosol formation during biomass combustion for various furnace and boiler types*. Fuel Processing Technology, 2007. **88**: p. 1136-1147.
5. Salby, M.L., *Physics of the Atmosphere and Climate*. 2 ed2012: Cambridge University press.
6. Susanne E. Bauer and S. Menon, *Aerosol direct, indirect, semidirect, and surface albedo effects from sector contributions based on the IPCC AR5 emissions for preindustrial and present-day conditions*. Journal of Geophysical Research 2012. **117**(D01206).
7. A. Abo Riziq, et al., *Optical properties of absorbing and non-absorbing aerosols retrieved by cavity ring down (CRD) spectroscopy*. Atmos. Chem. Phys., 2007. **7**: p. 1523–1536.
8. Poschl, U., *Atmospheric Aerosols: Composition, Transformation, Climate and Health Effects*. Angew. Chem. Int, 2005. **44**: p. 7520-7540.
9. Oleg Dubovik, et al., *Variability of Absorption and Optical Properties of Key Aerosol Types Observed in Worldwide Locations*. Journal of the Atmospheric Sciences 2001. **59**: p. 590-608.
10. H. Moosmuller, R.K. Chakrabarty, and W.P. Arnott, *Aerosol light absorption and its measurement: A review*. Journal of Quantitative Spectroscopy & Radiative Transfer, 2009. **110**: p. 844-878.
11. R. W. Bergstrom, et al., *Spectral absorption properties of atmospheric aerosols*. Atmos. Chem. Phys., 2007. **7**: p. 5937-5943.
12. Patrick Chazette and C. Lioussé, *A case study of optical and chemical ground apportionment for urban aerosols in Thessaloniki* Atmospheric Environment, 2001. **35**: p. 2497-2506.
13. McMurtry, P.H., *A review of atmospheric aerosol measurements*. Atmospheric Environment, 2000. **34**.
14. Ravi Varma, Hans Moosmüller, and W.P. Arnott, *Toward an ideal integrating nephelometer*. OPTICS LETTERS, 2003. **28**: p. 1007-1009.
15. Giel Berden, R.P.a.G.M., *Cavity ring-down spectroscopy: Experimental schemes and applications*. Int. Reviews in Physical Chemistry, 2000. **19**(4): p. 565-607.

16. Anders Pettersson, E.R.L., Charles A. Brocka, and A.R.R. Steven S. Brown, *Measurement of aerosol optical extinction at 532 nm with pulsed cavity ring down spectroscopy*. Journal of Aerosol Science, 2004. **35**: p. 995-1011.
17. L. E. Mack, E.J.T.L., S. M. Kreidenweis, D. Obrist, H. Moosmüller, W.P.A. K. A. Lewis, G. R. McMeeking, A. P. Sullivan, C. E. Wold, and J.L.C.J. W.-M. Hao, and W. C. Malm, *Optical closure experiments for biomass smoke aerosols*. Atmos. Chem. Phys. Discuss., 2010. **10**: p. 7469-7494.
18. Huffman, C.F.B.a.D.R., *Absorption and Scattering of Light by Small Particles* Wiley Science Paperback Series published 1998, ed. W. Science 1998: John Wiley & Sons, INC.
19. T. S. Bates, T.L.A., T. Baynard, T. Bond, O. Boucher, G. Carmichael, A. Clarke, C. Erlick, H. Guo, et al., *Aerosol direct radiative effects over the northwest Atlantic, northwest Pacific, and North Indian Oceans: estimates based on in-situ chemical and optical measurements and chemical transport modeling*. Atmos. Chem. Phys., 2006. **6**: p. 1657–1732.
20. Jacobson, M.Z., *Global direct radiative forcing due to multicomponent anthropogenic and natural aerosols* JOURNAL OF GEOPHYSICAL RESEARCH, 2001. **106**: p. 1551-1568.
21. Wriedt, T. SCATTPORT. [cited 2013 April 9]; Available from: <http://www.scattport.org/>.
22. J. Heintzenberg, et al., *Intercomparisons and Aerosol Calibrations of 12 Commercial Integrating Nephelometers of Three Manufacturers*. American Meteorological Society, 2006. **23**: p. 902-914.
23. Sarah J. Masonis, K.F., Albert Ansmann, Detlef Müller, and Dietrich Althausen, *An intercomparison of aerosol light extinction and 180 backscatter as derived using in situ instruments and Raman lidar during the INDOEX field campaign*. Journal of Geophysical Research, 2002. **107**.
24. P. J. Sheridan, A.J., and J. A. Ogren, *Spatial variability of submicrometer aerosol radiative properties over the Indian Ocean during INDOEX*. JOURNAL OF GEOPHYSICAL RESEARCH, 2002. **107**.
25. Ogren, T.L.A.a.J.A., *Determining Aerosol Radiative Properties Using the TSI 3563 Integrating Nephelometer*. Aerosol Science and Technology, 1998. **29**(1): p. 57-69.
26. Ogren, T.L.A.J.A., *Determining Aerosol Radiative Properties Using the TSI 3563 Integrating Nephelometer*. Aerosol Science and Technology, 1998. **29**: p. 57-69.
27. A Abu-Rahmah, W P Arnott, and H.M. Müller, *Integrating nephelometer with a low truncation angle and an extended calibration scheme*. Meas. Sci. Technol., 2006. **17**: p. 1723 - 1732.
28. J, D.B.T.a.F.P., *Discrete-dipole approximation for scattering approximations*. J. Opt. Soc. Am. A, 1994. **11**: p. 1491-9.
29. Y, X., *Electromagnetic scattering by an aggregate of spheres: asymmetry parameter*. Phys. Lett, 1998. **A**.
30. Y, X., *Radiative scattering properties of an ensemble of variously shaped small particles*. Phys. Rev, 2003. **67**(E): p. 046620.

31. T. Müller, et al., *Angular Illumination and Truncation of Three Different Integrating Nephelometers: Implications for Empirical, Size-Based Corrections*. Aerosol Science and Technology, 2009. **43**: p. 581-586.
32. T. Muller, et al., *Design and performance of a three-wavelength LED-based total scatter and backscatter integrating nephelometer*. Atmos. Meas. Tech., 2011. **4**: p. 1291-1303.
33. T. L. Anderson, D.S.C., S. F. Marshall, M. L. Laucks, R. J. Chalson, A. P. Waggoner, J. A. OGren, R. Caldow, R. L. Holm, F. R. Quant, G. J. Sem, A. Wiedensohler, N. A. Ahlquist and T. S. Bates, *Performance Characteristics of a High-Sensitivity, Three-Wavelength, Total Acatter/Backscatter Nephelometer*. American Meteorological Society, 1996. **13**.
34. Rachael E. H. Miles , S.R., Andrew J. Orr-Ewing & Jonathan P. Reid *Sources of Error and Uncertainty in the Use of Cavity Ring Down Spectroscopy to Measure Aerosol Optical Properties*. Aerosol Science and Technology, 2011. **45**: p. 1360-1375.
35. TSI, *Model 3563 Integrating Nephelometer, in Operation and Service Manual* 2005.
36. P. Massoli , D.M.M., D. A. Lack , T. Baynard , C. A. Brock b & E. R. and Lovejoy, *Uncertainty in Light Scattering Measurements by TSI Nephelometer: Results from Laboratory Studies and Implications for Ambient Measurements*. Aerosol Science and Technology, 2009. **43**: p. 1064-1074.
37. N. Lang-Yona, Y.R., E. Segre, E. Dinar, and A. Abo-Riziq, *Complex Refractive Indices of Aerosols Retrieved by Continuous Wave-Cavity Ring Down Aerosol Spectrometer*. Anal. Chem., 2009. **81**: p. 1762-1769.
38. Christa A. Hasenkopf , M.R.B., Melissa G. Trainer, H. Langley Dewitt, Miriam A. Freedman , Owen B. Toon , Christopher P. McKay, Margaret A. Tolbert *Optical properties of Titan and early Earth haze laboratory analogs in the mid-visible*. Icarus, 2009: p. 903-913.
39. Huaxin Xue, A.F.K., Lin Wang, Jun Zheng, and Renyi Zhang, *Effects of Coating of Dicarboxylic Acids on the Mass-Mobility Relationship of Soot Particles*. Environ. Sci. Technol., 2009. **43**: p. 2787-2792.
40. Alexei F. Khalizov, H.X., Lin Wang, Jun Zheng, and Renyi Zhang, *Enhanced Light Absorption and Scattering by Carbon Soot Aerosol Internally Mixed with Sulfuric Acid*. J. Phys. Chem., 2009. **A(113)**: p. 1066-1074.